June 24, 2007

Search for Magnetic Monopoles at the Relativistic Heavy Ion Collider (RHIC)

Praveen Chaudhari*, Peter Cameron, Nicholas D'Imperio, Vasily Dzhordzhadze, Veljko Radeka, Margareta Rehak, Pavel Rehak, Sergio Rescia, Yannis Semertzidis, John Sondericker, and Peter Thieberger

Brookhaven National Laboratory

ABSTRACT

Dirac showed that the product of electric and magnetic charge is quantized. Since then (1931), there have been numerous searches for magnetic monopoles. To date there has been no definitive proof that a monopole exists. The searches can be classified into two broad categories: cosmic monopoles predicted by the Grand Unified Theories (GUT) and monopoles produced in accelerators.

We propose a new detector to search for monopoles produced in an accelerator, by collisions between gold ions at 100 GeV per nucleon in the Relativistic Heavy Ion Collider at Brookhaven National Laboratory. We propose to detect the monopoles using the one property that defines them, namely their quantized magnetic charge. In designing of our detector we make no assumptions (unlike all previous accelerator-based searches) about the mass, the binding energy to matter, the velocity, or the magnitude of the charge of the monopole. We accomplish this by having neither material nor magnetic field between the point of production of monopoles and the detector.

Our detector uses a superconducting inductive loop, arranged in a gradiometer geometry, which is coupled to a superconducting quantum interference device (SQUID). The SQUID responds to the current induced by the magnetic charge of a monopole and measures directly its magnitude, independently of the speed of the monopole. Pairs or more of these detectors provide for coincident detection schemes to rule out spurious magnetic signals. In addition, a silicon detector is placed behind the gradiometers and is used to monitor and measure the energy loss of particles produced by collisions.

* Spokesperson

TABLE OF CONTENTS

EXECUTIVE SUMMARY..... p.3

1. THE PHYSICS MOTIVATION…….. p.5
2. ELECTROMAGNETIC FIELDS PRODUCED BY RHIC BEAMS... p.11
    2.1 MAGNETIC FIELDS……..…… p.11
    2.2 EARTH'S MAGNETIC FIELD……..…… p.12
    2.3 ELECTROMAGNETIC EFFECTS…….…… p.12
3. GRADIOMETER AND DETECTOR…… p.14
    3.1 GRADIOMETER…….. p.14
        3.1.1 MUTUAL INDUCTANCE BETWEEN GRADIOMETERS … p.15
        3.1.2 CONSTRUCTION OF GRADIOMETERS..... p.17
    3.2 SQUID DETECTOR..... p.17
        3.2.1 SQUID ELECTRONICS..... p.20
    3.3 EXPERIMENTAL VERIFICATION..... p.20
    3.4 SILICON DETECTOR..... p.22
    3.5 MONITORING DEVICES.....…..... p.25
4. DATA ACQUISITION AND TRIGGER.....…….…..... p.25
    4.1.TRIGGERS AND MONITORS…….…… p.25
    4.2.DATA RECORDING…….…. p.27
5. INTERACTION OF CHARGED PARTICLES WITH SQUIDS..... p.27
6. INFLUENCE ON RHIC BEAMS FOR PHENIX AND STAR..... p.28
7. CRYOSTAT AND DETECTOR ASSEMBLY..... p.29
    7.1 CRYOSTAT p.29
    7.2 ARRANGEMENT OF GRADIOMETERS AND GRIDS..... p.31
    7.3 CRYOGENICS: HEATING AND COOLING..... p.32
        7.3.1 HEAT LOADS..... p.32
        7.3.2 COOLING..... p.34
8. FUTURE DEVELOPMENTS p.35
9. SCHEDULE..... p.36
10. COSTS..... p.37
11. REFERENCES.....p.38

APPENDIX
    A.1 SECONDARY ELECTRONS..... p.40
    A.2 THERMAL ANALYSIS..... p.45
    A.3 STRUCTURAL ANALYSIS..... p.46
    A.4 MAGNETIC SHIELDING..... p.49

EXECUTIVE SUMMARY

In electromagnetism, the counterpart to the electron is the magnetic monopole. Dirac showed that the monopole charge g is ($1/2\alpha = 68.5$) n e, where α is the fine structure constant, n is an integer, and e is the electric charge of the electron. No monopole detection has ever been confirmed. There is no theoretical argument to rule out the presence of monopoles and in some theories, such as Grand Unified Theory (GUT), the existence of a monopole is obligatory.

Masses of monopoles are expected to range from a few GeV (some expect the lower bound to be ~1TeV) to 10^{17} GeV; the higher end associated with GUT monopoles. There is no field theory model for the production of monopoles in accelerators. In recent years, the approach has been to estimate monopole production cross sections as a function of the monopole mass by employing the Drell -Yan mechanism for dileptons production, where the dilepton is replaced by a monopole-antimonopole pair. It is recognized that the coupling constant for monopoles, unlike that for electrons, is substantially larger than one and hence currently available predictions of monopole mass or their cross sections are questionable. In certain models the large self monopole coupling requires it to have a lower mass limit of ~1 TeV, which will be accessible at the LHC. It is for this reason that monopole searches have been carried out, since 1959, at every new accelerator that has gone into operation with the notable exception of the Relativistic Heavy Ion Collider (RHIC).

No monopole has been detected in any accelerator based experiment. There can be two reasons for the absence of a monopole signal. No monopoles were produced or, alternatively, the assumptions made by the researchers about the properties of monopoles in the design of their detectors were not appropriate. These assumptions include the mass of a monopole, its quantum of charge, binding energy to matter, and velocity. Here, we propose to build and test a prototype detector that makes no assumption about the properties of a monopole other than its defining property --- that it has a magnetic charge.

We accomplish this by placing several superconducting inductive detectors in coincidence inside the chamber where the collisions take place with a clear line of sight between the collision point and the detectors. This experimental arrangement, as far as we know, has never been used before in accelerator based monopole searches. In addition, a silicon detector is placed behind the inductive detectors and is used to monitor and measure the energy loss of particles produced by collisions.

We propose to test our prototype detector using heavy ions (e.g. Au-Au collisions at 100 GeV per nucleon) at RHIC. We plan to use the collision intersection at 10 o'clock (the former PHOBOS site). We have no special beam requirements and will run in passive mode with the two big experiments: PHENIX and STAR.

It is possible that the RHIC beam energy per nucleon may not be sufficient to produce monopoles and, hence, we may see no monopole generated events in our SQUID

based detector. However, we will have demonstrated the functioning of a new type of detector in the high energy accelerator environment and this will enable us to approach the management of the Large Hadron Collider (LHC) to continue our search there.

1. THE PHYSICS MOTIVATION

Monopoles are predicted by the Grand Unification Theories (GUT) of the electroweak and strong interactions, as topological defects formed during the GUT phase transition [1].

Dirac [2] showed that the product of electric and magnetic charge is quantized. As the magnitude of the electrical charge, e, of an electron is known to be quantized, it follows that the magnetic charge, g, of the monopole is also quantized and has a value given by $g = n\hbar c/2e = 68.5ne$, where n is an integer, ħ the reduced Planck's constant, and c the velocity of light. We note the charge strength of the monopole is substantially larger than that of an electron.

There is remarkable symmetry between electric and magnetic fields. But Maxwell's equations, which capture the essence of electromagnetism, are not symmetric with respect to electric and magnetic charge. If a monopole can be demonstrated to exist then these equations would be symmetrical.

Hence, there is strong motivation to search for monopoles. These searches have indeed been carried out over the last five decades but no monopole sighting has been unambiguously established. The searches can be divided into two broad categories: cosmic monopoles, produced during GUT or later phase transitions, and accelerator based monopoles produced by high energy collisions between electrons or nucleons.

The GUT monopoles are expected to be massive: 10^{17} GeV if produced during the first phase transition, and substantially less if produced in subsequent phase transitions. In contrast, String Theories predict masses in the tens of TeV range. The heavier mass GUT monopoles are expected to be slow moving with $\beta \ll 1$ and are best detected using superconducting inductive detectors, which are velocity independent. Lighter mass monopoles can be accelerated by intergalactic magnetic fields to relativistic speeds but to date no event has been confirmed to be associated with a monopole [3].

There are more than thirty publications on accelerator based searches for monopoles. In the following, we discuss various aspects of the experimental sensitivity using approaches widely adopted in this research community. We note, however, the reliability of the theories underlying these approaches is not clear. We present four aspects of monopole production at accelerators.

1. Monopole production cross sections as a function of monopole mass by the Drell-Yan mechanism.
2. Theoretical prediction of monopole masses.
3. The cross section and mass limits achievable at RHIC and LHC.
4. Comparison of these cross sections with existing experimental data.

1. *Monopole production:* There is no field theoretical model for the production of monopoles. The most widely used model is the Drell-Yan mechanism, where the dilepton is replaced by a pair of oppositely charged monopoles. We have used the methodology of Gavin et al [4] for dilepton production using perturbative QCD. Dr. Werner Vogelsang of this Laboratory has developed his own code [5] for producing Drell-Yan cross sections using next-to-leading order perturbative QCD and parton distribution functions (in this case "CTEQ6M") integrated over parton cross sections. He has calculated the cross sections for dilepton production, integrated over all rapidity. He has subsequently integrated these $d\sigma/dM$ cross sections from an assumed monopole-antimonopole mass to $\sqrt{s}$, and included in his integration the effect of the Z boson resonance, and the β^3 [6] dependence used in computing monopole cross sections. These results are then multiplied by $(ng/e)^2 = 4692.25$, where we have set n=1, g and e are the monopole and electron charges respectively, to obtain the cross sections for monopole productions. We show the results in Fig. 1 for pp, AuAu, and Lead-Lead (PbPb) collisions appropriate for RHIC and LHC energies.

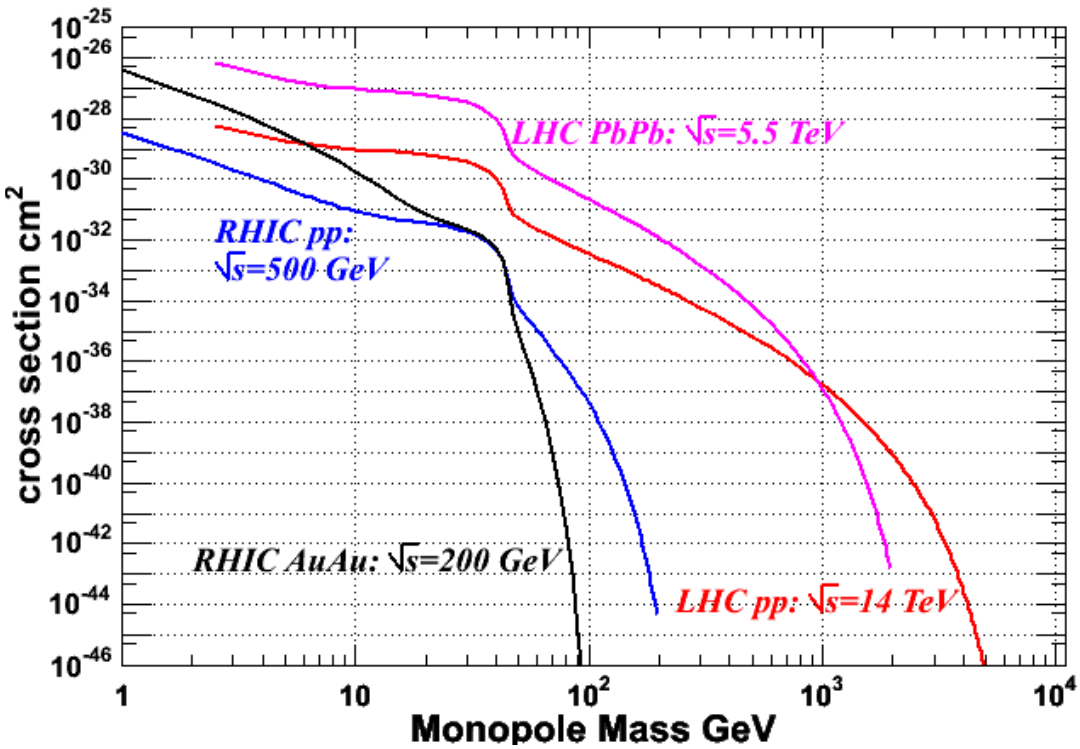

Figure 1. Calculated monopole cross sections produced by the Drell-Yan mechanism for RHIC at 500 GeV (pp), 200 GeV/nucleon (AuAu), and LHC 14 TeV (pp), and 5.5 TeV/nucleon (PbPb). The shoulders in the cross section curves originate from the Z boson contributions to the cross sections.

2. *Monopole masses:* From an experimental perspective it is highly desirable to have a theoretical prediction of the mass of a monopole. Using the Drell-Yan mechanism of monopole production, we could then design an optimal experiment. Unfortunately, there is great latitude in the choice of a mass of a monopole. We list in Table 1, the mass or mass limits proposed in the literature. The assumptions of the theory underlying the mass limits proposed by the three virtual processes, listed in the table, have been questioned [7].

Table 1. Magnetic Monopole Mass Predictions and Limits based on Theoretical assumptions.

Process	Mass Limit, GeV	References
Electron radius	= 2.4 GeV	
g-2 muons	> 240	22
High Pt γ 's	> 610, s = 0	23
High Pt γ 's	> 870, s = ½	23
High Pt γ 's	> 1580, s=1	23
Z -> $\gamma\gamma\gamma$	> 400	24
Electroweak MM	~ 50 – 10^4	25
Superstring	~ 10^3 -10^5	26
GUT	~ 10^{16} - 10^{17}	27

3. *Cross sections versus mass:* The calculations for cross section limits for pp collisions for both RHIC and LHC are straightforward, as we know the values of the expected integrated luminosities. Assuming a detector efficiency of 50%, we obtain the cross sections shown in Fig. 2. (We emphasize that the feasibility detector proposed here has an acceptance efficiency of 0.5%). Experiments with heavy ion collisions can result in much lower cross section limits than obtained from nucleon collisions because of the Z^4 term [8]. We show the results of the calculations by Dr. A. Baltz [9] and, for masses below approximately 10 GeV this is indeed what he finds for AuAu collisions at RHIC. We show this in Fig. 2. In Fig. 3 we have plotted the LHC projected Drell-Yan cross section prediction and expected cross section limits at 95% confidence level for the pp and PbPb interactions.

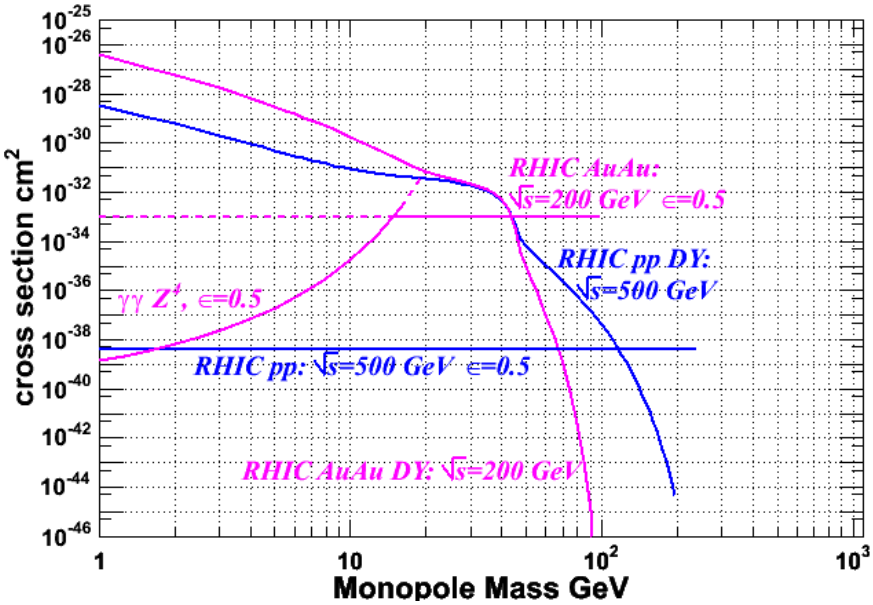

Figure 2. Calculated monopole cross sections produced by the Drell-Yan mechanism and expected cross section limits at 95% CL (horizontal lines) for pp, √s = 500 GeV (blue) and Gold-Gold, √s = 200/n (pink) interactions at RHIC. The pink curve includes the cross section limits calculated for γγ interactions (Z^4 enhancement) occurring in Gold-Gold interactions.

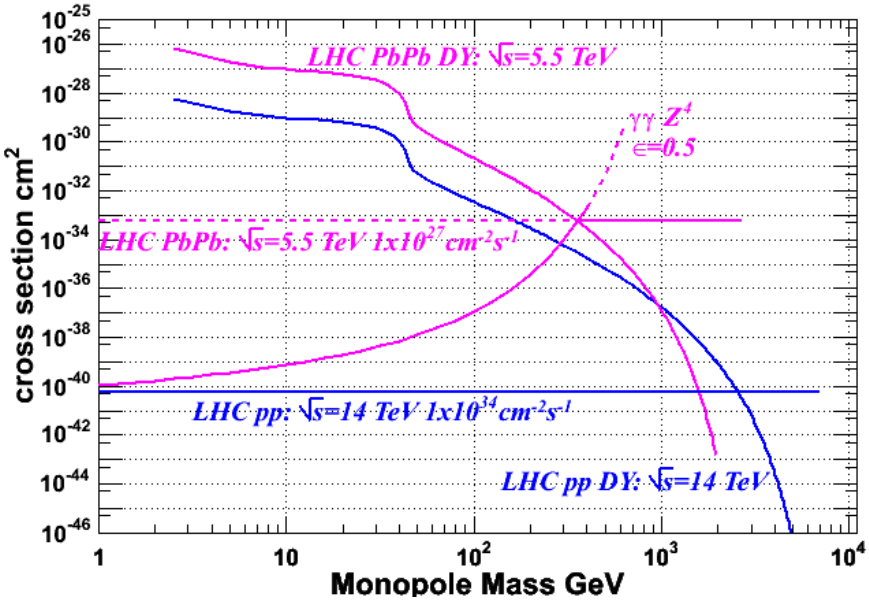

Figure 3. Calculated monopole cross sections produced by the Drell-Yan mechanism and expected cross section limits at 95% CL (horizontal lines) for pp, √s = 14 TeV (blue) and Lead-Lead √s = 5.5/nucleon (pink) interactions for the LHC. The pink curve includes the

cross section limits calculated for γγ interactions (Z^4 enhancement) occurring in Lead-Lead interactions.

4. *Comparison with published experimental searches:* We plot in Fig. 4 and Fig. 5 the published cross section limits as a function of monopole mass [10]. We have superimposed the projected cross sections achievable at RHIC and LHC, shown in Figs. 2 and 3 above. We have multiplied the integrated gold luminosity by 231 and the lead by 256, as per Dr. D. Kharzeev [11], to take into account the number of nucleons involved in AuAu or PbPb collisions. We note that by using proton beams at RHIC we could set the lowest cross section limits for monopole masses approaching 250 GeV or just over 100 GeV, if monopoles are produced by the Drell-Yan mechanism and our predicted cross sections are valid.

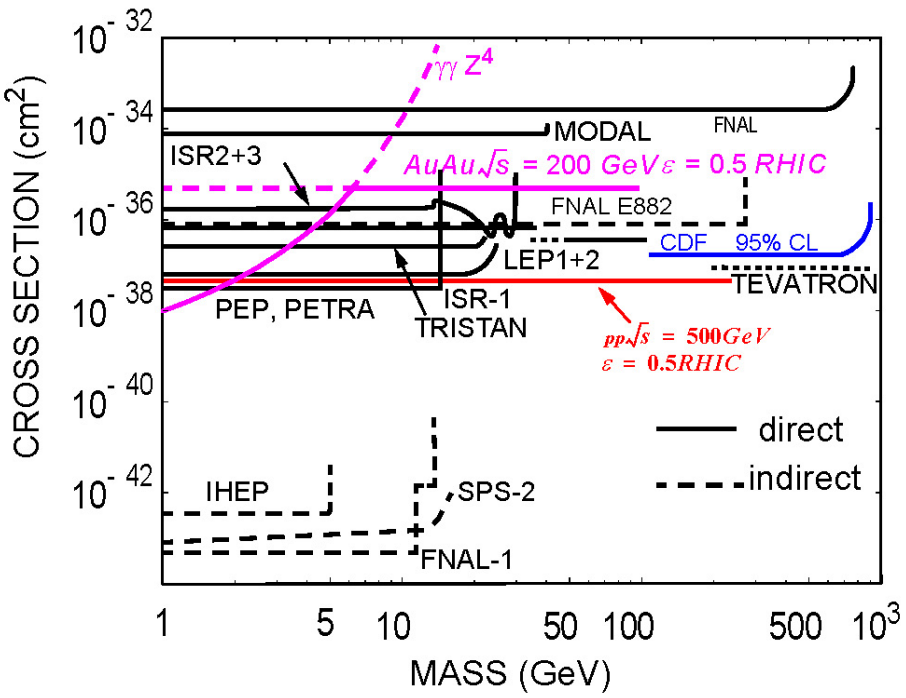

Figure 4. Classical Dirac magnetic monopole cross section upper limits versus magnetic monopole mass obtained from direct accelerator searches (solid lines) and indirect searches (dashed lines) taken from ref. [10] with RHIC projected cross sections.

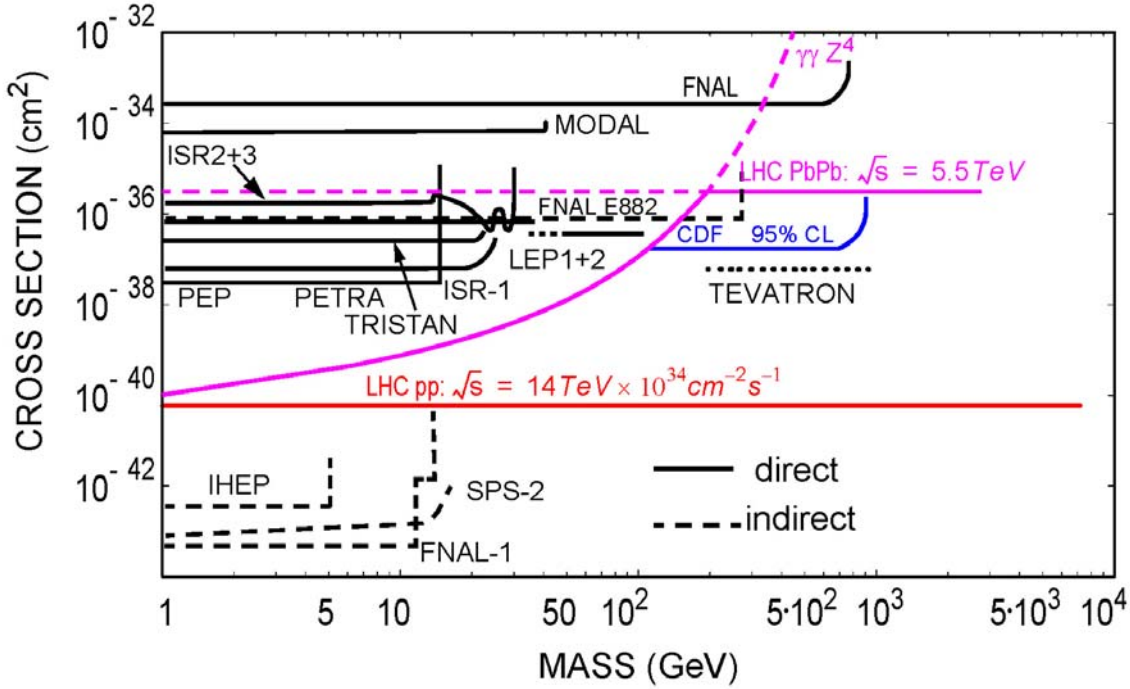

Figure 5. Classical Dirac magnetic monopole cross section upper limits versus magnetic monopole mass obtained from direct accelerator searches (solid lines) and indirect searches (dashed lines) taken from ref. [10] with LHC projected cross sections.

There have been close to three dozen experiments on monopole searches at accelerators. Each of these searches assumed some property of the monopole in designing their detector. We will not describe the assumptions of every published experiment. However, we discuss four experiments: three from FNAL [12, 13, and 15] and one from IHEP [14]. Two of the FNAL experiments have been published within the last two years and the third along with the IHEP more than 30 years ago, and they hold the records for the lowest cross sections for fixed targets.

The two most recent experiments from the FNAL are designed with very different assumptions about the properties of monopoles and their interaction with matter. The first by Kalbfleisch et al [12] asserts that all monopoles produced in collisions at the intersection point are trapped in the metal tube, such as Al, surrounding it. The experiment by the CDF group [13] is based on the assumption that the monopoles pass through the tubes and other intervening materials with sufficient velocities to excite a scintillator. Both sets of experiments have magnetic fields parallel to the beams and both assume values of the monopole charge such as to assure that they are not swept away from their detector area. For example, in the case of the CDF experiment the magnetic field sweeps all monopoles away from the detector if the quantum number of charge of the monopole is greater than one. (If the fundamental unit of charge is e/3 rather than e, no monopole is expected to reach the detector). The two older experiments assume that monopoles produced in Al, stainless steel, and iron targets, are trapped inside the targets.

In the case of iron by its magnetic moment and in the case of Al it is assumed that the monopole diffuses through the Al solid and collects on the surface. It is further assumed that with the application of a magnetic field the monopole is pulled away from the trapped site and accelerates before striking the scintillator. We note the assumptions made by these older experiments are very different from those of Kalbfleish et al [12] where the monopole is trapped by the nuclei and so strongly bound that it cannot be pulled away by the type of fields used in the older experiments.

A detector system that shares a common vacuum with the collision point, and therefore has no material in the path of a monopole, obviates the need to assume the binding property of a monopole with matter. By having no magnetic field at the collision point we can also avoid assuming the magnitude of the charge of the monopole. Finally, by having a velocity independent detector we can detect magnetic monopole relying only on its most important characteristic, the magnetic charge. If we combine all of these requirements, the only practical detector we know of today is the one we are proposing: that of using a superconducting quantum interference device (SQUID) coupled to a sensing element such as superconducting gradiometer. While simple in concept, it is difficult to implement given the harsh accelerator environment. Hence the proposal to build a detector that demonstrates feasibility before embarking on a full detector.

The challenge now is in the design of a highly sensitive superconducting detector in the very demanding environment of high-energy accelerators. These challenges can be summarized as follows:

Shielding against magnetic fields generated by circulating charged particles, stray magnetic fields, including the earth's magnetic fields, and their variation in time; radiation damage; cooling of the detector to below the superconducting transition temperature; secondary radiation induced by particles or radiation generated during RHIC collisions; and avoiding impact on the operation of RHIC for the two large experiments.

In what follows, we address each of these challenges and propose a design for an accelerator based superconducting detector that we believe will work.

2. ELECTROMAGNETIC FIELDS PRODUCED BY RHIC BEAMS

2.1. MAGNETIC FIELDS

The attenuation required for the magnetic fields originating from the beam itself will be achieved by placing both normal and superconducting shields, in the form of grids, between the RHIC collision point and the SQUID detector. A normal conducting copper grid will be placed over the opening in the beam pipe, to carry image currents and provide the first layer of shielding. A second grid, biased at – 500 V will be next and the purpose of this grid is to prevent the electrons from the beam pipe slit from reaching the superconducting detectors. In addition, the gradiometer and the SQUID will be totally enclosed by a superconducting cylinder and two superconducting grids on either end (see Figure 13, p.29) forming an excellent magnetic field shield. The DC magnetic fields are

totally screened from the gradiometer by the Meissner effect and the AC magnetic fields are screened by the two copper grids and the very good reflective properties of superconductors. The design of a superconducting shield is described in a later section. This approach only works if we do not exceed the critical fields of the superconductor; in our case, niobium.

Hence, we estimate below the magnetic fields generated by RHIC beams. We find these fields are orders of magnitude below the critical fields of niobium. Our shielding should therefore be more than adequate in this regard.

The magnetic field induced by the passage of the beam particles is $B = \frac{\lambda}{2\pi\varepsilon_0 c}\frac{\beta}{r}$ where λ is the line charge density, $\beta = v/c$, is the particle's velocity divided by the speed of light, and r is the distance of the gradiometer from the beam location. The circumference of RHIC is 3834m. With 110 bunches of ~10^9 heavy ions (HI) (Au, Z = 79) per bunch, the average line charge density assuming a continuous charge distribution is ~ 4.6 pC/m, and the DC magnetic field ~1m away from the beam pipe is ~ B_{DC} = 20nT. With ~9.4 MHz bunching frequency, the bunches are ~32 m apart. With beam captured at store in the 197 MHz cavities, the root mean squared (rms) bunch length is σ =~1 nsec, or 0.3 m. The magnetic field resulting from bunching is then $l/2\sigma$ ~50 times larger, or B = 1μT.

In RHIC there are two counter-rotating beams generating magnetic fields which cancel to first order. In the preceding estimate we had assumed just one beam. With colliding bunches the resulting fields will cancel to the extent that the bunch charges are equal and bunches are properly longitudinally aligned at the collision point.

2.2 EARTH'S MAGNETIC FIELD

With three parallel layers of μ-metal shields we can reduce the earth's magnetic field by a factor of 10^3 to 10^4. These shields are now followed by two superconducting shields, which pin the magnetic field such that the variation in magnetic field at the detector plane is minimized. It is expected that the background magnetic fields are sufficiently reduced so that any fluctuations in this field by moving metallic objects or motion of vortices in the superconducting shields can be handled by the gradiometer.

2.3 ELECTROMAGNETIC EFFECTS

There are two sources of EM fields which can degrade the functioning of our superconducting detector. One of these is associated with the beam profile and the other with collisions.

In the case of a Gaussian longitudinal profile the 3dB point of the spectrum of bunches with rms bunch length of ~1nsec would be ~130 MHz. Intrabeam scattering with

gold ions smoothes out longitudinal 'hot spots', and the actual spectrum does not depart significantly from Gaussian. In order to provide a direct line of sight between the interaction point and the gradiometer, and at the same time keep the electrical continuity in the vacuum chamber seen by the beam particles, we intend to use two fine metallic meshes at and near the vacuum chamber opening. The combination of these two grids plus the superconducting grid shield should provide attenuation of the ~130 MHz coherent spectrum of 200dB or better. The beam magnetic field at the gradiometer should then be < ~1pT. For this field the area capturing one flux quantum is ~2000 mm^2. The portion of the coherent spectrum of the beam that passes through the shielding can be rejected by the gradiometer. The beam Schottky spectrum is down ~100dB from the coherent spectrum. However, it extends much higher in frequency, and is more difficult to shield. The effect of the beam Schottky spectrum is under study.

We believe the three grids we propose to use can attenuate most of the electromagnetic disturbances emanating from RHIC collisions. There is a strong possibility, however, that the intensity of some frequencies in the EM spectrum may be sufficiently intense that additional screening may be essential, such as an additional rf shield in the form of a honeycomb structure or planar fins, which are placed parallel to the slit at the intersection diamond.

We plan to measure, as much as possible, the frequency spectrum of the EM produced by RHIC. We also plan to simulate the propagation of EM waves through our system. We plan to use the BNL code Maxwell Solver and Simulator (Maxssim). Maxssim is a parallel, scalable, finite difference time-domain (FDTD) code capable of simulating various electrodynamics problems of interest. The code can handle complex geometry as well as realistic initial and boundary conditions including finite size effects which are implemented through absorbing boundary conditions using the Perfectly Matched Layer (PML). The code also has the capability to model the effects of particle beams of various configurations, intensities and energies.

The simulations are very computationally intensive and will require very large computing resources due to the three dimensional nature of the problem as well as the varying length scales of the components. For example, fine mesh screens must be modeled in a computational domain measured in meters. BNL has recently acquired a 100 TFLOP IBM Blue Gene L supercomputer which we plan to use to perform the simulations. We have already initiated the simulations.

It is quite likely that there will be excitation of the superconducting shielding box by charged particles produced by Au-Au collisions. This signal can be sufficiently attenuated in our design by decreasing the Q-value of the cavity with the use of a stainless steel detector tube and the support of gradiometers within the superconductive shielding cylinder. Moreover, the geometry of the gradiometers is optimized to reject signals due to the interaction of the magnetic field (of the fundamental component of the excitation of the cavity) with imperfections of geometry.

3. GRADIOMETER AND DETECTORS

3.1 GRADIOMETER

A magnetic monopole (i.e. magnetic charge) traversing a conductive loop ("pick-up coil") causes a change in flux across the loop and induces a current, Im = $\Delta\phi/L_{loop}$, that can be detected. The change in flux induced by a monopole is $2\ \phi_0$, where $\phi_0 = 2.07 \times 10^{-15}$ *Wb* is the flux quantum. In order to detect such a minuscule signal, it is essential to have a very low noise environment. We plan to achieve this by a combination of magnetic and superconducting shielding used in conjunction with a superconducting pick-up loop arranged in a gradiometer geometry.

The use of a superconductor reduces Johnson noise, the magnetic shielding reduces and substantially locks the magnetic field, and the spatial variations in magnetic field caused by random changes in the flux across the superconducting loop are minimized by suitable gradiometer geometry.

An external μ-metal shield around the entire cryostat and a superconducting shield enclosing the pick-up coil-SQUID assembly are employed (see Figure 13, p.29) This arrangement, as discussed later, reduces by many (up to four) orders of magnitude the magnetic fields from the earth, neighbouring equipment, or RHIC, sensed by the detector loop. However, as the detector is cooled to liquid helium temperature the small residual magnetic field is trapped within the superconducting shield. This trapped flux in the shield, present in the form of vortices, can be subject to random motion due to changes in temperature, vibration, or EM fields, and hence induce spurious signals in the pick-up coil, which can, in principle, be indistinguishable from a monopole signal. In order to minimize the signal from these variations in magnetic field while keeping the full monopole signal we use a planar gradiometer. We discuss briefly the operation of the gradiometer and its geometry.

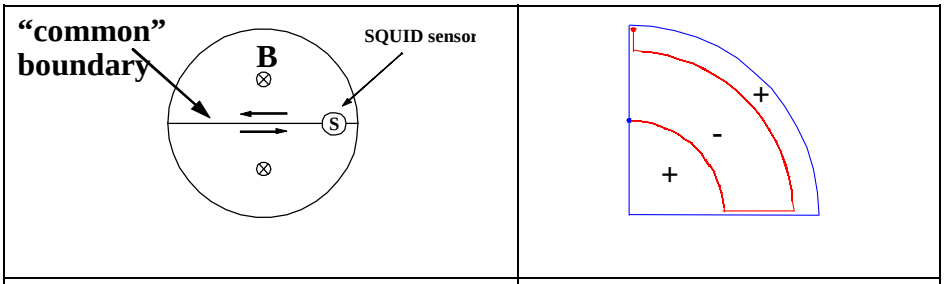

Figure 6a: First order gradiometer	Figure 6b: Second order radial gradiometer

The pick-up coil in a first order gradiometer as shown in Figure 6a above is divided into two equal top and bottom semicircles. A uniform magnetic field induces currents of opposite polarity in the common boundary and therefore no resultant current flows through the SQUID sensor. In contrast a monopole traversing either loop will generate the full current. A higher order gradiometer, such as the radial second order gradiometer shown in Figure 6b, cancels the first derivative of the spatial variation of the magnetic field [16]. Its wiring layout is obtained by continuously bending the "common boundary" to subdivide the gradiometer area into "cells" where positive or negative currents are induced by the time varying magnetic field [17].

However, increasing the order increases the length of the wires used in the gradiometer and therefore the inductance. An increase in inductance results in a smaller current to the SQUID and hence a smaller signal. There is, therefore, a tradeoff between the order of the gradiometer and inductance. Three gradiometer designs under consideration are show below (Table 2) along with their calculated inductances. In computing the values, we have used the gradiometer wiring scheme for reducing inductances [17]. We have verified that our computed values are correct by experimentally measuring the inductance of a mock gradiometer.

3.1.1 MUTUAL INDUCTANCE BETWEEN GRADIOMETERS

Along the lines of the preceeding discussion we plan to use a coincidence detector arrangement to eliminate spurious signals by placing two gradiometer detectors in parallel. However, this scheme only works if the two detectors are practically independent (i.e. not coupled magnetically). We have computed the mutual inductance between the two second order gradiometers as a function of their distance and the results are shown in Table 3.

Table 2: Inductance of various high order gradiometers

Geometry	Type	L [μH] (calculated)
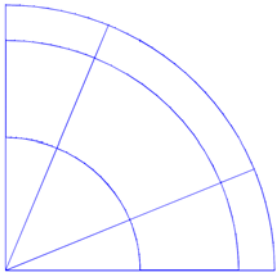	2nd order gradiometer (3x3 sections in R and φ)	0.98
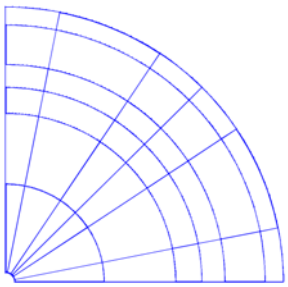	3rd order gradiometer (6x6 sections in R and φ)	1.9
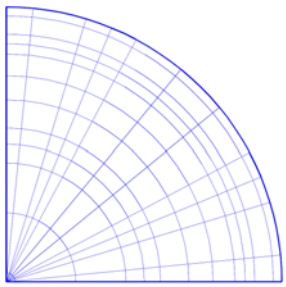	4th order gradiometer (11x11 sections in R and φ).	3.1

Table 3: Mutual inductance between gradiometers

Distance in z[mm]	Mutual Ind [nH]	Coupling coeff k
50	11.1	18.6E-3
100	2.36	3.9E-3
150	0.82	1.4E-3

Note: For a shorted inductor the coupling coefficient (linked magnetic flux) is also the ratio of currents when only one inductor is excited.

For our proposed experiment, even with a 50 mm spacing only 0.2% of any signal induced in the first inductor will appear in the second. We plan to use 10 cm spacing. The question isn't so much if a current in one gradiometer will induce a significant current in the other, as what a common electromagnetic disturbance will do to both. From this last point of view a larger separation is desirable.

3.1.2 CONSTRUCTION OF GRADIOMETERS

As mentioned before, the gradiometer coil will be superconductive. The coil can be lithographically patterned by depositing a naobium film on a suitable substrate. The substrate must be thermally conductive in order to cool the niobium coil to below its superconducting transition temperature as it is the substrate which is in thermal contact with the 4.2 K cryostat walls at its boundary. Since a goal of this experiment is to have no material between the collision point and the detectors, most of the substrate material has to be removed and the niobium metal lines will be on narrow ribs of material. A suitable substrate material is a commercially available as a 30 cm diameter single crystal silicon wafer, which shows good thermal conductivity (better than Cu at 4.2 K). Laser cutting or chemical etching are well known technologies for removing Si and we will explore both for our purposes. As the final structure might appear to be subject to flexing, we have calculated the mechanical properties of the etched-out substrate. We discuss the mechanical properties in Appendix A3.

Each plane will be divided into four quadrants with their own SQUIDs. There are three reasons for choosing this arrangement rather than using one SQUID per plane. First, this reduces the inductance per gradiometer by a factor of four thus enhancing the signal to noise ratio. Second, it gives us some redundancy in case radiation damage is greater than anticipated. And third, any external disturbances (e.g. a magnetic field change) which cause a coincident signal in more than one gradiometer in the same plane will be rejected.

The signal from the gradiometer-SQUID detector will be calibrated using a pseudopole, which will be incorporated as part of the detector system. This will enable us to calibrate the system during operation. A pseudopole is a finely wound helical coil, which threads one of the loops of the gradiometer and closes on itself to produce no measurable external field. However, the vector potential produced by a calibrated current induces a signal in the superconducting loop equal to that of a monopole.

3.2 SQUID DETECTOR

The gradiometer pick-up coil is connected by means of an input coil to a superconducting quantum interference device (SQUID). The SQUID and input coil are integrated on a single crystal silicon "washer" (usually square, a few millimeter long for

the large SQUID necessary in our application). The input coil-SQUID assembly must be magnetically shielded and is enclosed in a small niobium box (approximately 1.5cm diameter and 5-6cm long). These devices are availble commercially.

An external magnetic field B causes a flux change in the pick-up loop $\Delta\phi_p$. In the folowing L_p , L_i, L_s are the inductances of the pick up loop, the input loop, and the SQUID. This flux change induces a current I_S in the series connection of the pick-up and input loops such that:

$$\Delta\phi_P + (L_P + L_i)\cdot|I_S| = 0 .$$

The flux coupled into the SQUID is:

$$\Delta\phi_S = M_i \cdot \frac{\Delta\phi_P}{L_P + L_i} .$$

where $M_i = k_i\sqrt{L_P L_S}$ is the mutual inductance between the input coil and the SQUID (the coupling coefficient k_i is close to unity for an integrated washer-type SQUID).
The SQUID noise properties are described by its spectral flux noise density $\phi_{n,S}$ (of dimension $Wb/\sqrt{Hz}$). The SQUID magnetic flux noise spectrum is white, with a *1/f* noise component at frequencies less than 10-100 Hz for DC SQUIDs, as is reported in the literature [18].

The spectral flux noise density referred to the pick-up coil becomes:

$$\phi_{n,P}(f) = \frac{L_P + L_i}{k_i\sqrt{L_P L_i}} \cdot \phi_{n,S}(f) .$$

The minimum noise condition is achieved when $L_p = L_i$ as can be verified by equating to zero the derivative of $\phi_{n,P}$ with respect to L_i. For this optimum condition, the flux noise density referred to the pick-up coil is:

$$\phi_{n,P(opt)}(f) = \frac{2}{k_i} \cdot \sqrt{\frac{L_P}{L_i}} \cdot \phi_{n,S}(f) .$$

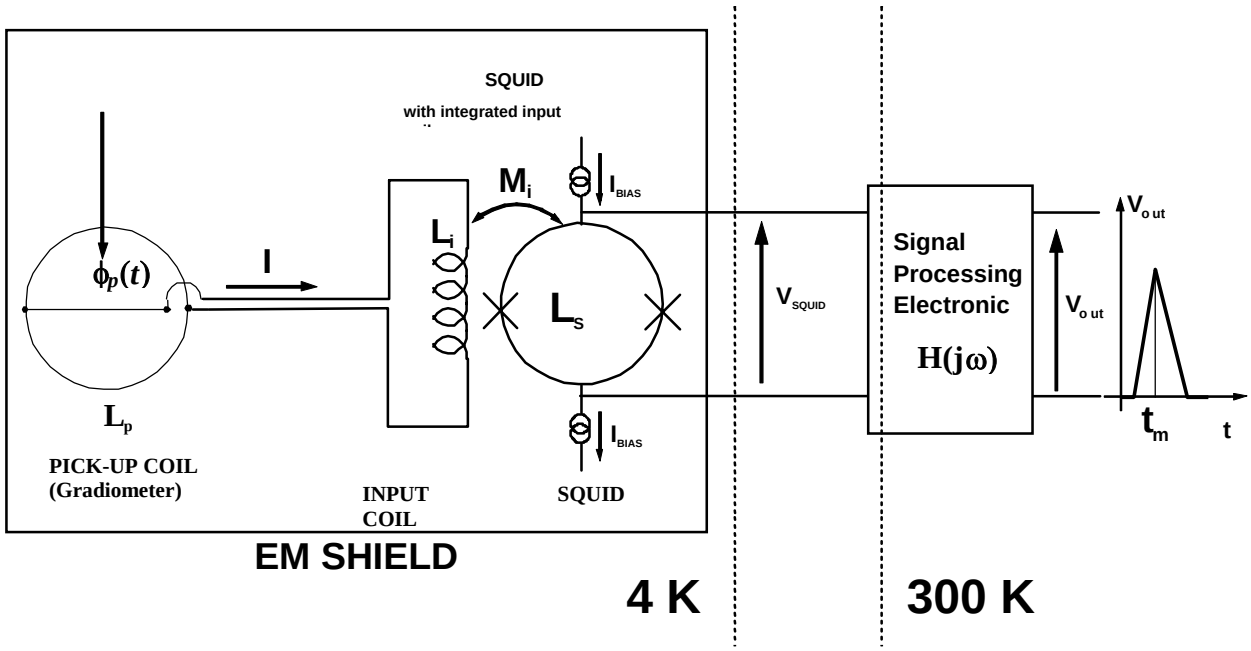

Figure. 7: Gradiometer-SQUID system for noise calculation.

The total noise is obtained by integrating the spectral noise density over the measurement bandwidth. It is best expressed as an *"equivalent noise flux"* (ENF) referred to the pick-up coil, and defined as the change in flux which would cause an output signal at the measurement time equal to the rms noise measured at the output (i.e. the magnetic flux change necessary to achieve a signal to noise ratio of one). Disregarding the *1/f* noise (which would give a small contribution in a wide bandwidth measurement system), it can be calculated for the optimum noise condition of $L_p = L_i$ and assuming a triangular shape for the output signal peaking at the measurement time t_M :

$$ENF \cong 2.8\phi_{n,S}\sqrt{\frac{L_P}{L_S}}\cdot\frac{1}{t_M} \ .$$

The inductance of a gradiometer coil can be limited to 2-3 μH by subdividing the full gradiometer into smaller sections (e.g. into four quadrants). Large SQUIDs reported in the literature have an input coil inductance of ~ 2 μH, a SQUID inductance of 300-500 pH and achieve a noise $\phi_{n,s} = 5 \times 10^{-6}\ \phi_0/\sqrt{Hz}$ where $\phi_0 = 2.07 \times 10^{-15}\ Wb$ is the flux quantum.

Under these assumptions the ENF achievable for 100 μs measurement time is ~ $0.03\ \phi_0$. This would allow a coincidence resolution between the two gradiometers and the silicon detector of a few microseconds. The triple coincidence between the two SQUID gradiometers and the ionization detector would be a powerful signature for rejection of spurious events.

3.2.1 SQUID ELECTRONICS.

Most commercially available SQUID readout systems are designed for sensing small magnetic fields for material characterization or for biomagnetism studies (magnetocardiograms, magnetoencephalograms, and etc.) and have bandwidths of a few kilohertz. Large bandwidth systems have been described in the scientific literature [19] and are also available commercially (Magnicon GMBH, Germany and Tristan Technology, San Diego, Ca). We shall work with a vendor to acquire the appropriate electronics. A moderately high bandwidth in the 10-100kHz range would allow monopole signal shaping with a filter, such that unwanted signals at low frequencies are strongly attenuated. This will result in a lower sensitivity to signals caused by mechanical vibrations of the detector components.

3.3 EXPERIMENTAL VERIFICATION

We have built two third-order gradiometers and two magnetometers and are currently testing them in the RHIC environment at the former BRAHMS intersection point. The devices are housed in a liquid helium dewar shielded with three layer of mu-metal. The two third order gradiometers and a magnetometer of the same area (and the readout SQUIDs) are further shielded by a double layer lead box, simulating the superconducting shielding box proposed for the experiment. In addition we have a small integrated SQUID-magnetometer assembly outside the shielding box to monitor the magnetic

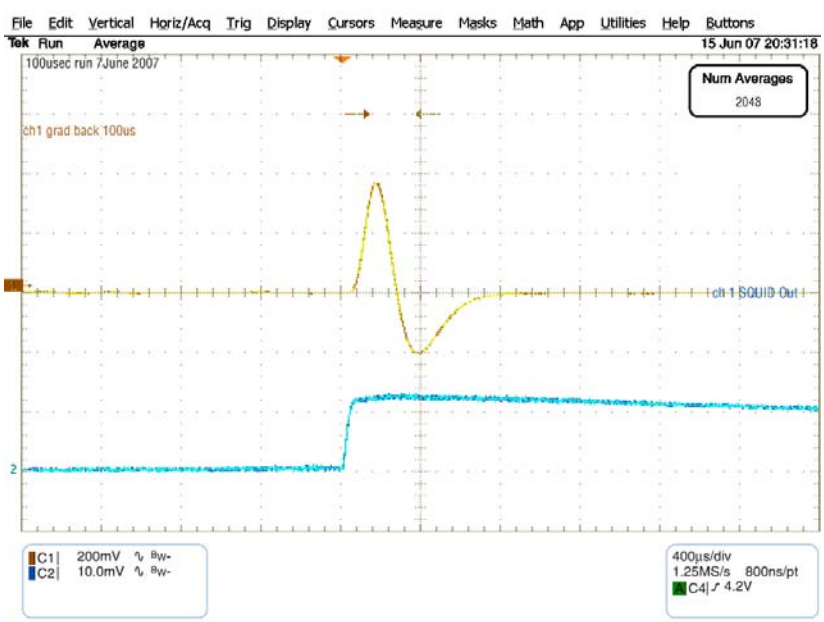

Figure 8: BNL SQUID response to a $5\Phi_0$ magnetic flux calibration signal injected by means of a pseudopole. Blue trace is the SQUID output and the yellow trace is the filtered waveform to improve *S/N* ratio.

disturbances penetrating inside the shielded dewar which might generate a synchronous signal in the gradiometers. The output of the SQUIDs is monitored continuously, both during AuAu collisions and during periods of collider inactivity.

The purpose of these tests was two fold: familiarize ourselves with the RHIC electromagnetic and radiation environments, and test the operation of the gradiometers and SQUIDs, and although imperfect shielding and excessive low frequency noise has so far prevented achieving a resolution low enough to be able to detect a $2\Phi_0$ monopole signal, the experiment has largely demostrated that SQUID can operate near the interaction point of a particle collider (see figures 9).

Fig 8 shows a $5\Phi_0$ signal in the SQUID, which was injected by a calibrated pseodopole.

Figure 9 shows a typical noise spectra detected by the SQUID for two cases: when the system was not in a beam (green spectrum) and when SQUIDs were in the beam of heavy ions (AuAu, 200 GeV/n energy, red spectrum).

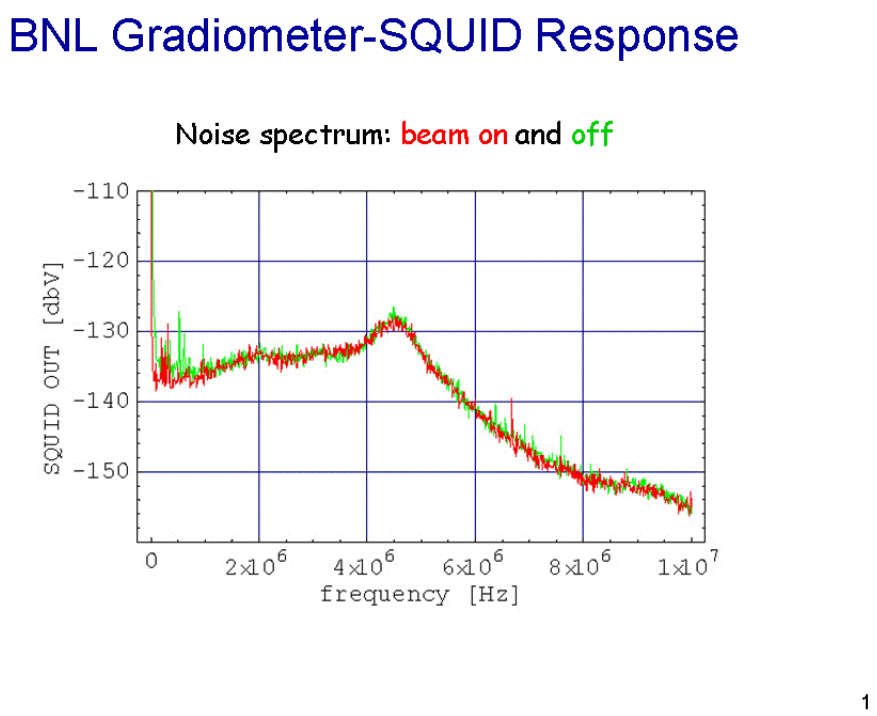

Figure 9. A typical SQUID noise signals without beam (green spectrum) and with a beam (AuAu 200 GeV/n, red spectrum).

3.4 SILICON DETECTORS

Two planes of thin silicon detectors follow the two gradiometers. There are four reasons to place silicon detectors within the experimental set-up.

1) The ionization signal created by the passage of a monopole having $\beta > 10^{-3}$ through the silicon detection plane in coincidence with the gradiometer signals decreases substantially the probability that a background disturbance would mimic a real monopole detection (only a slower moving monopole will trigger both gradiometers but produce nothing in a silicon detector).

2) Measurements of the ionization produced by a magnetic monopole in both planes of silicon can clarify the statistics of the ionization process in a non-perturbative region of the interaction of monopoles with matter.

3) To identify and reject any possible collective effects of particle showers in gradiometers.

4) Silicon detectors are sensitive to normal charged particles produced by collisions at RHIC, and will serve as a continuous monitor of the experimental set-up.

The geometry of silicon detectors follows from the geometry of the gradiometers (Figure 10). Ideally, we would like to follow all individual loops of gradiometers with individually read silicon detectors. Given the proximity to the superconductive elements at liquid helium temperature, silicon detectors have to work at temperatures between 4 K and 40 K. The read out electronics should be at or close to room temperature. A read-out system having one channel per detector segment would require too many feed-throughs from the high-vacuum low-temperature detector, through the insulating vacuum and into the ambient atmosphere. The heat conductivity of all the connection wires would present a larger heat load to the cooling system than the sum of all other losses. We have to adopt a more modest read-out system which nevertheless provides all required information about the ionization losses in silicon.

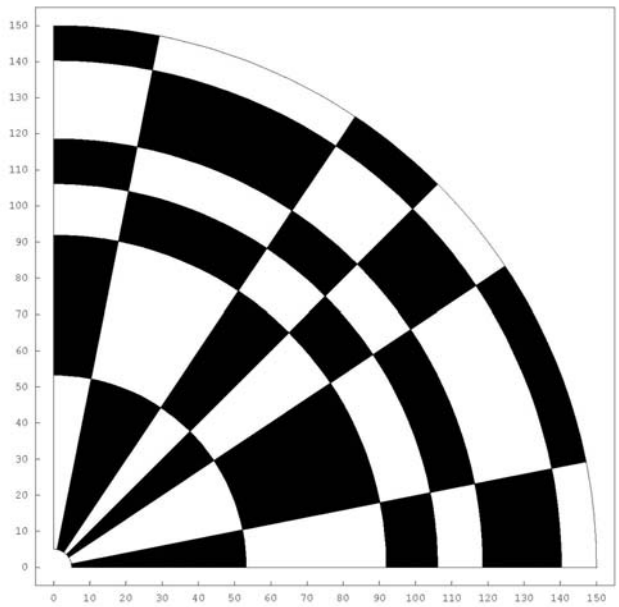

Figure 10. Geometry of silicon detectors.

Figure 11 shows a quarter of a third order gradiometer in one detection plane. The geometry of a gradiometer of any degree is topologically equivalent to a chessboard

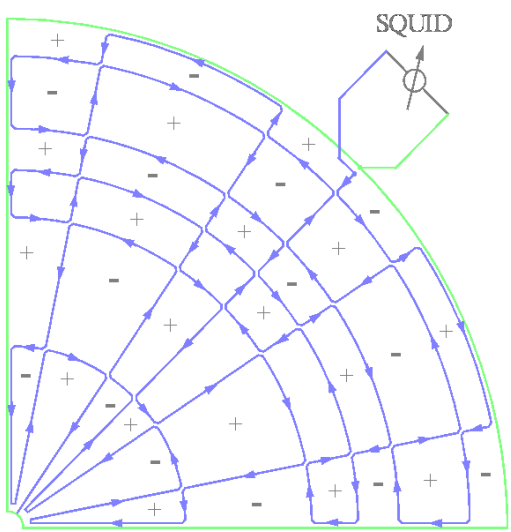

Figure 11. One quadrant of the third order gradiometer.

where black squares loops induce a current in one direction and white squares in the opposite direction in the SQUID read-out when traversed by a magnetic charge of a given

polarity. The gradiometer of the third order contains 144 loops. Each loop is followed by an individual silicon detector. We can connect 96 detectors following smaller loops in 48 groups each carrying signals from 2 smaller area detectors of the same color in parallel and have 48 individual detectors following larger loops bringing the total number of channels to 96. Only one feed-through for bias voltage is required in this simple read-out scheme keeping the number of feed-through connection below 100 per plane.

A single plane of a fourth order gradiometer contains 484 loops. The simple read-out scheme possible for a third order gradiometer will require too many feed-through in this case and a more complex connection logic is required. In this scheme, we will take a signal from each detector twice. Each silicon detector has two electrodes called here the low and the high voltage electrode and ionization produces the same size signal of opposite polarity in high and low voltage electrodes. We plan to connect together the low voltage electrodes of 11 silicon detectors following the "chessboard" squares of one color in one direction and to connect the 11 high voltage electrodes following the same color "chessboard" squares in the other direction. The return current of the high voltage side is provided by the low voltage side and no additional feed-throughs are needed. Thus, we need 44 low voltage connections and 44 high voltage connections, that is 88 in total for one plane. The silicon system, which has two detection planes, can be accommodated with a total of 200 feed-through connections for a gradiometer of any order under consideration here.

The connection scheme considered here is similar to that used for well-known double-sided strip detectors where instead of strips we have arrays of individual detectors. The challenge with silicon detectors is the performance at low temperature and their ability to be tested at room temperature. The performance at low temperature requires heavy dose implants on both sides of silicon and the contacts between the implanted layers and the metal on the top of the implantation regions have to be very good. The ability to test at or close to room temperature requires a long lifetime from carriers in silicon and a good quality of rectifying contacts. In the following description, we will assume the thickness of silicon detectors to be 400μm. This is a commonly used thickness in commercially available high resistivity wafers for silicon detectors.

The area covered by 11 detector segments connected together is about $15cm^2$, leading to a total capacitance of a read out channel of about 500pF including stray capacitance in the connections. The signal charges of interest start at a charge produced by the passage of a Minimum Ionizing Particle (MIP) equal to 32 000 electron hole pairs, up to several times the expected charge produced by the passage of a monopole with n=1, generating 5000 MIPs when β approaches 1. To see a single MIP the Equivalent Noise Charge (ENC) should be only a small fraction of one MIP defining the dynamic range of 10^5 or about 16 bits. The required precision of the charge measurements is less than 10 bits. To accommodate the large dynamic range with a modest cost of electronics we will implement the two-slope preamplifier approach [20], which suppresses the dynamic range already at the output of the preamplifier by a factor of 100 and allows the use of a standard 10 bit electronic read-out for the rest of the system.

Let us estimate the noise of a read out channel to see if a single MIP can be detected. We will assume a modest noise performance from the preamplifier expressed by the voltage noise spectral density of $3nV/Hz^{1/2}$ and a modest readout speed defined by a shaper output of a symmetrical triangular form with a peaking time of 2 μs. The ENC of the individual read out channel is 6600 electrons rms, giving a signal to noise ratio $S/N = 5$ for a *MIP*. The ratio is not high enough to trigger on MIPs, however, individual particles should be easily visible when a trigger is provided from a different channel. It is not difficult to detect a signature ionization of a monopole with n=1 and its location within one detector ("chessboard square"). There may be some ambiguity in the location of individual MIPs when the silicon detectors are flooded with showers of particles produced upstream. These events are rare, and when identified could be rejected without the need for a perfect reconstruction.

3.5. MONITORING DEVICES

Given the sensititvity of the detector system to external perturbations, we plan to monitor, on a continuous basis, the local magnetic field, RF fields, local vibrations, the occurrence of sudden impact (accelerometers), and temperature of a number of components.

4. DATA ACQUISITON AND TRIGGER

4.1.TRIGGERS AND MONITORS

We have to be certain that the detection system does not miss any monopoles passing through the gradiometers during the entire duration of the data taking. This implies that 1) the apparatus must register any signal from the two gradiometers which may suggest a passage of a monopole and 2) the apparatus has to be functioning with a minimum of dead time.

Accordingly, we plan to have two kinds of triggers and event types. The first type of trigger registers all information about possible candidate events and the second type of trigger monitors the performance of all parts of the apparatus.

The main trigger of the first type is mainly based on signals from the gradiometers. The rate of triggers of this kind is expected to be low enough that an OR signal from the two gradiometers will cause the read-out of the full apparatus. We will OR the SQUID trigger and a trigger coming from silicon detectors. When an ionization signal from a single silicon detector is observed and if it exceeds ionization produced by about 200 charged particles we shall assume that this event can be interpreted as ionization produced by the passage of monopole with $\beta>0.05$. There are practically no "standard" events with such a high multiplicity of charged particles within a 10^{-4} fraction of the total solid angle corresponding to a single silicon detector and the rate of these events is low enough to be included as an OR from both planes in the first type of trigger.

We list below the second type of trigger. We will include all triggers after suitable pre-scaling in a logical OR.

a) Trigger on a clock pulse from RHIC indicating the crossing of beams in the intersection region. This clock has a frequency of 10 MHz and has to be pre-scaled by about a factor of 10^9 to keep the total trigger rate within reasonable limits.

b) Trigger on coincidence between the RHIC clock and signal slightly above the noise floor of any SQUIDs. This trigger has to be pre-scaled down by a factor of the order of 10^6 to limit its writing rate. This trigger will monitor the performance of SQUID read out.

c) Trigger on coincidence between the RHIC clock and a signal produced by a few charged particles in any silicon detector. This trigger will be pre-scaled down by a factor of the order of 10^6 to limit the writing rate. These events are typical events produced by Au-Au interaction and we can take advantage of their detailed knowledge to monitor the performance of the silicon system and of the noise level in the SQUIDs read out electronics.

d) Trigger on coincidence between the RHIC clock and a signal produced by several charged particles in each plane of silicon detectors. This trigger has to be pre-scaled down by a factor of the order of 10^3 to limit its writing rate. These triggered events roughly correspond to central collisions of Au-Au interactions and are again well studied by other RHIC experiments. We will be able to identify background events and learn enough about them to be able to eliminate the kind of events mimicking a monopole signal.

e) Trigger on coincidence between the RHIC clock and a signal above the noise floor but below the monopole signal of any SQUIDs. This trigger has to be pre-scaled down by a factor of the order of 10^3 to limit its writing rate. This trigger will provide an additional monitoring of the performance of SQUID read out.

f) Trigger on coincidence between the RHIC clock and signals produced by several hundreds of charged particles in each plane of silicon detectors. The thresholds in signals from silicon detectors will be high enough that this trigger requires only a modest pre-scaling by a factor of the order of 10. This kind of the trigger is already close to the first kind of trigger based on the ionization produced by fast monopoles.

g) Trigger on coincidence between the RHIC clock and a signal right below a monopole signal from any SQUIDs. The threshold will be adjusted at the level that this trigger needs to be pre-scaled down only by a factor of the order of 10 to limit its writing rate. This kind of the trigger is already close to the first kind of trigger based on signals from SQUIDs.

We will use the RHIC luminosity monitoring to obtain the integrated luminosity for our experiment.

4.2. DATA RECORDING

Independently of the kind of trigger, the event record will contain information from all components of the apparatus written in a pre-determined format. Some examples include:

1) Event heading: run number, event number, time information through the beam–beam scaler or equivalent, status of apparatus (temperature of various sensors etc.) type of trigger which is responsible for the event. We estimate that the header will not be longer than about 512 bytes.

2) Waveforms from all 8 SQUIDs from about 1ms before the crossing of interest to about 1 ms after the crossing with the sampling interval of 10^{-6} second. Assuming 8 bit ADCs the length of this information is 16000 bytes.

3) Waveform samples from all 200 silicon channels sampled about 10 times around the time of the interaction. We may use 10 bit ADC with a sampling frequency of 10 MHz giving us less than 3000 bytes of information

The total length of an individual event is only about 20 kB. If we keep the writing rate at about 0.1 Hz the rate of writing data to a disk will be only 2kB/sec. Given this low data rate, the data acquisition and monitoring could be done on a PC.

5. INTERACTION OF CHARGED PARTICLES WITH SQUIDS AND CHAMBER WALLS

It has not been experimentally established to what extent, if any, the superconducting tunnel junctions in the SQUIDs produce signals if they are traversed by charged particles. There is only one publication [19], which suggests that there is no effect. However, its relevance to our geometry is not clear. This question may, however, be moot given the very low probability of incidence of the charged particles on the very small SQUID junctions. The highest expected density (multiplicity) of charged particles produced in central Au-Au collisions at the location of the flux detectors is less than 120 charged particles per steradian (see Appendix A1). For a 10x10 μ junction at 1 meter this gives a probability of a single incidence of $\sim 10^{-10}$, and therefore of two coincident events of $\sim 10^{-20}$ (i.e. negligible over the course of the experiment).

We have verified our expectation by placing a SQUID housed in a commercial Dewar next to the intersection point at the former BRAHMS site during the current run and seen no change in the functioning of the SQUID. We show the results in Fig. 12. Here we plot the maximum and minimum of the current oscillations as a function of an external magnetic field. The period between the oscillations corresponds to a superconducting flux quantum. We observe no change in the amplitudes of these currents as a function of time during the RHIC run.

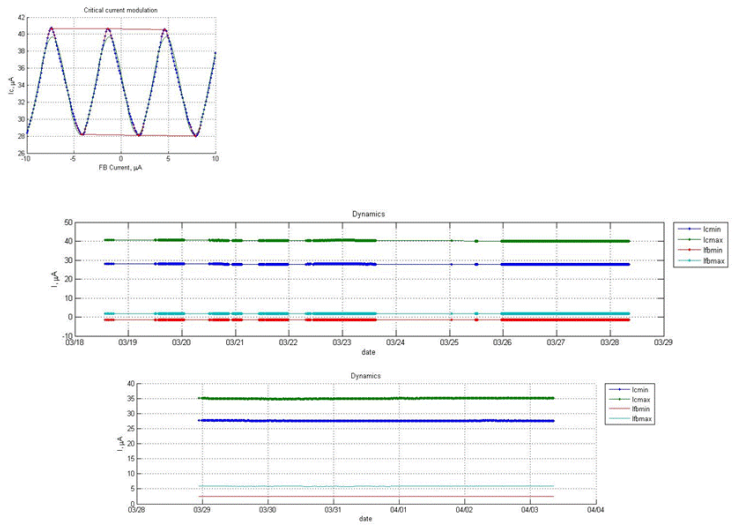

1

Figure 12. The SQUID amplitudes during the RHIC operation.

One of the concerns that we have is the generation of secondary particles or radiation produced by the products of RHIC collisions when they impinge on the walls of the chamber surrounding the SQUID detectors. Such secondary radiation can, in principle, increase the noise to an unacceptable level. We have estimated this effect and concluded it is not a serious problem. We present our calculations in Appendix A1.

6. INFLUENCE ON RHIC BEAMS FOR PHENIX AND STAR

As will be evident from the detailed description of the detector assembly, below, our experiment requires sharing the RHIC vacuum. It also requires that we make a cut in the 10cm beam pipe in the intersection region to enable a monopole to reach the gradiometer without traversing any solid material in its path. We plan to cover the slit in the beam pipe by plated Cu grids. This will minimize RF disturbances for both RHIC operation and our detector.

In order to prevent any impact on RHIC vacuum by a loss of vacuum in our detector, we will place an automatic vacuum valve at the entrance of our chamber that closes on high pressure to protect RHIC beam pipe vacuum. The placement of this valve is shown in Figures 13 and 14, presented in the following section. In addition, two 100 mm valves will be placed in the RHIC beam tube either side of the experiment. Should a vacuum problem in our detector arise, and we expect the probability of this to be very low, we can remove our entire beam pipe assembly and replace it by a pre-baked pipe, so that RHIC can continue to operate.

7. CRYOSTAT AND DETECTOR ASSEMBLY

The preliminary design phases of the cryostat and refrigeration systems have been completed and the path to final design and construction is clear. Next to be accomplished is a survey of the 10 o'clock hall environment for anything that could have an influence on the monopole experiment. Plans are under way to remove PHOBOS, a RHIC experiment presently located at 10 o'clock, and when cleared work can begin to measure the earths and stray magnetic fields along with an assessment of any vibrations found via long term monitoring. Measurements of the area have been made to determine available space vs. space needed. Ample space is available in the tunnel and a large trailer parked outside, previously used by PHOBOS, is more than sufficient for a control room and data handling.

7.1 CRYOSTAT

The outer vessel of the cryostat is a stainless steel vacuum tank which, along with super-insulation blankets and a refrigerated radiation shield, will be pumped to $<10^{-4}$ Torr to reduce radiant and conductive heat to the 4.2K surfaces. Figure 13 is a cross section drawing of the cryostat.

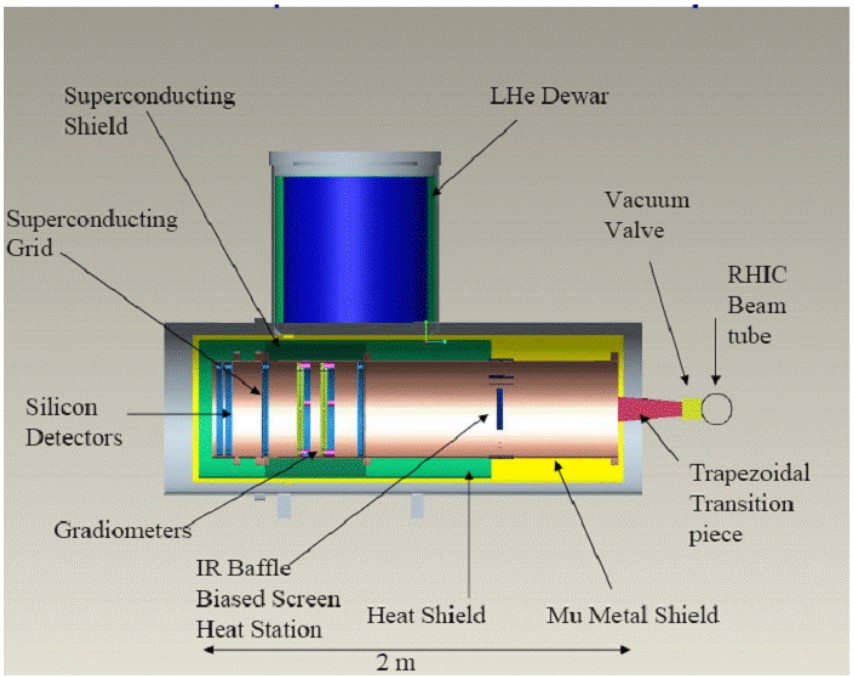

Figure 13. Cross Section of the monopole detector cryostat.

The upper cylinder contains its own thermal shielding and a 225 liter LHe supply Dewar (blue in color) which is the source of all refrigeration for both primary (4.2K level) cooling and cooling of secondary heat shielding elements. The Vacuum vessel measures 36” (914 mm) in diameter and 74" (1900 mm) in both length and height.

The lower horizontal part of the vacuum vessel houses triple isolated mu-metal shields to reduce DC and low frequency magnetic fields around the detector. Going inward, more super-insulation, a refrigerated heat shield (green color) and more super-insulation blankets. Near the inlet end of the 16" (406 mm) diameter, .040" (1mm) wall beam tube, a cooled heat sink/baffle absorbs off axis infrared radiation (IR) and heat conducted from the ambient temperature RHIC end of this experiment. From the baffle to the silicon detectors, the experiment's beam tube vacuum is cryo-pumped by the low temperature of the surrounding walls. But from the baffle to the vacuum stop valve, wall temperature rises to 300K which means having to bake the warm end. Baking at 150 ^{o}C over a 24 hour period is standard procedure to reduce out gassing so that experiment vacuum levels equal or exceed those of the RHIC beam tube. Because the high temperature would damage mylar superinsulation, the heated section of beam tube is insulated using layers of aluminum foil separated by nomex, a high temperature cloth. A line up of the various elements of the experiment in beam tube is displayed in Figure 14.

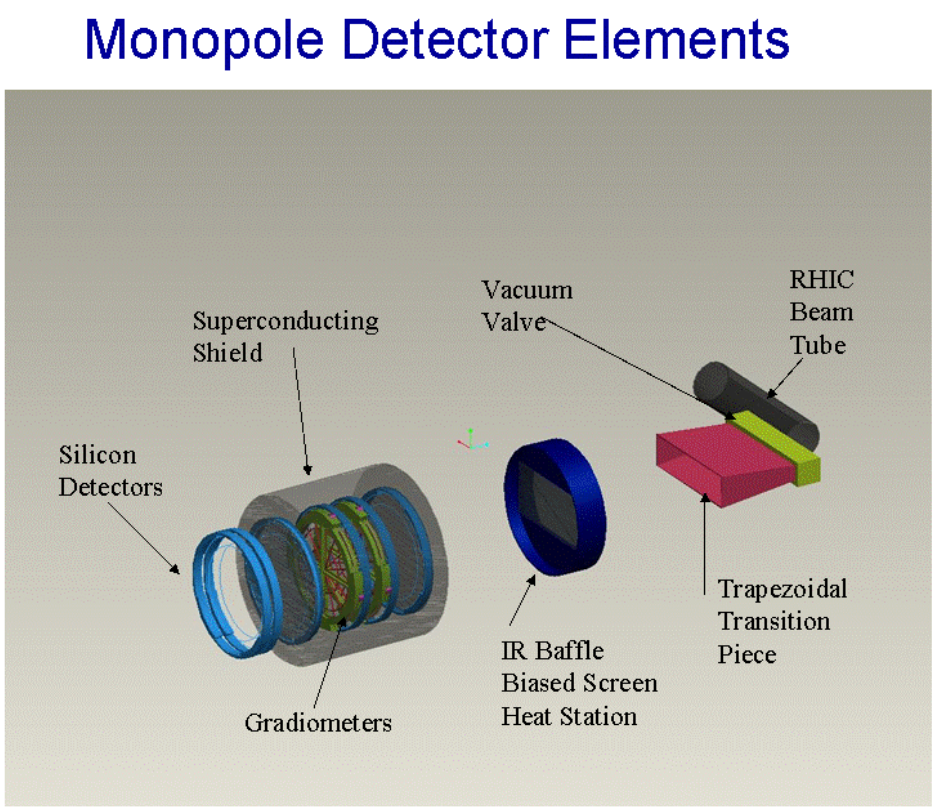

Figure 14. View of the Experiment Beam Tube Elements.

In addition, an electrically biased central screen is placed in the opening of the baffle to deflect electrons away from the detectors produced by the RHIC beams. The far right side of figure 14 shows the 4" (100 mm) RHIC beam tube. Just outside the beam tube is a valve which can isolate the detector from the RHIC beam tube vacuum.

Another step inward brings one to the plenum for LHe, which is gravity filled from the storage vessel above. Two gradiometers and eight SQUIDs are mounted to and cooled by the inner wall of the plenum, all surrounded by a superconducting (SC) box. At the far end of the experiment beam tube there are two silicon detectors.

7.2 ARRANGEMENT OF GRADIOMETERS AND GRIDS

The drawing below, Figure. 15, shows the gradiometer and its assembly.

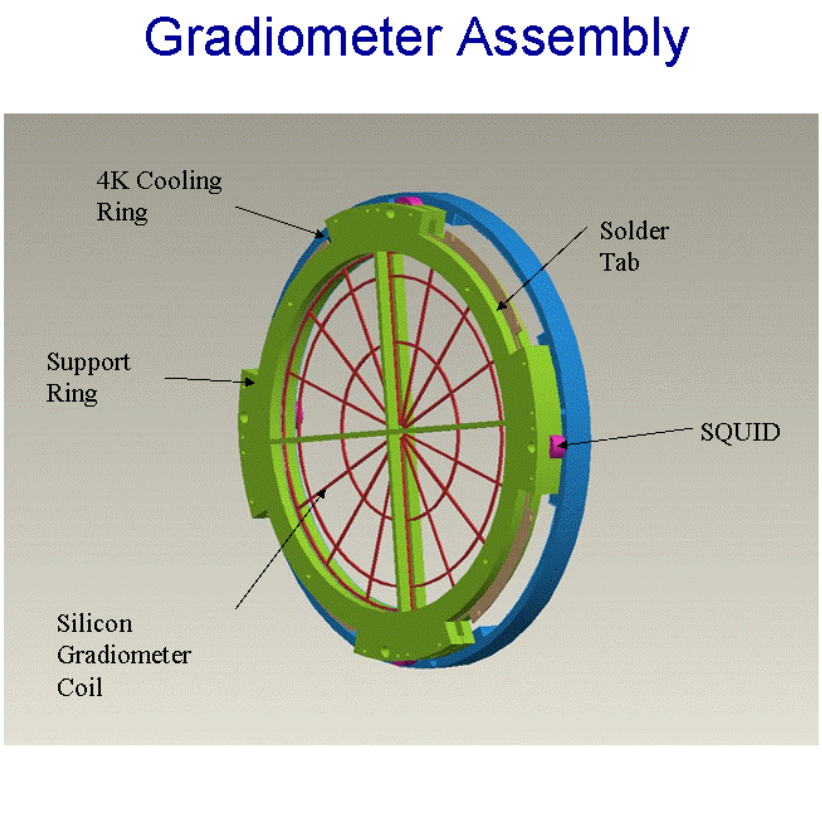

Figure 15. Gradiometer Assembly.

The red gradiometer coil grid is 300 mm in diameter, assembled as four quarter pie shaped pieces. Each section coil conductor is 2 X 3 mm copper clad silicon strip coated with niobium superconductor. The mechanical frame (green) has to not only hold

these pie shaped pieces firmly in place but must also provide a means to cool the niobium to near 4.2K and not crack the thin and brittle pick-up coil. The blue band shown above partially penetrates the wall of the inner plenum cylinder and is in contact with liquid helium. Computer simulation (ANSYS) and hand calculations have shown that two copper braids, soft soldered to the tab of a silicon pie bring the temperature of the central point to within 0.5K of the outer edge with an IR heat load of 24W/m^2 (Appendix A.2). One gradiometer disk utilizes four low temperatures (LT) SQUIDs each connected to a quarter coil. Since LT SQUIDs must be cooled to approximately 4.2K, the gradiometer SQUIDs (shown in red above) are surrounded by LHe temperature surfaces assuring proper operating temperature.

The green cross stiffener, shown above, has been added to decrease the likelihood of vibration by tying the four quarters together for support and stabilization. An example is shown in the Appendix A.3.

Figures 13 and 14 show two superconducting grids placed parallel to the gradiometers and which close the ends of the SC box. A grid design, we are considering, is the use of 1mm thick copper stock, etching 1 cm square holes with spacing between holes of 0.5 mm and then depositing niobium on its front edge surface. ANSYS modeling showed that with an IR heat load of 2.4 W/m^2 central cooling by conduction produced a 1 K temperature rise across the radius of the grid; a very acceptable solution.

7.3 CRYOGENICS: HEAT LOADS AND COOLING

7.3.1 HEAT LOADS

Given the sensitivity of the SQUIDs to external perturbations, it is desirable to keep the frequency of LHe fills to a minimum. We have opted for one fill a day as the minimum acceptable requirement.

The monopole experiment will be refrigerated by boiling liquid which implies that the primary load (at the 4.2K level) will get its refrigeration exclusively from the heat of vaporization. Secondary cooling of heat shields and beam tube heat sinks will use the specific heat of the boil off gas as it is warmed from 5K to near 80K. The LHe storage vessel has a volume of 225 liters of which 175 liters can be boiled off by the heat load; the remainder is reserved as a buffer at a pressure of about 1.1 atmospheres.

Using 175 liters in 24 hours or 7.3 liters/hour we can remove 5.1 Watts of a primary heat load and with the 0.25 g/s of gas boil off flow cool a secondary heat load (from 5K to 80K) of 100 Watts.

We now estimate the heat loads of our proposed experimental arrangement. Many of our calculations are based on equations that use ideal parameters. Furthermore, poor design and construction methods can only add to the heat load. We shall therefore add margins where there is uncertainty.

Primary Heat Load Estimate - Heat that causes boiling of LHe

LHe Plenum Heat Load:

Conduction losses	Electrical wiring	.50 Watt
	Beam tube	.80 "
	Supports	.20 "
IR losses	Exp. Beam Tube	.90 "
	Multilayer Insulation heat leak, 80K to 4K	.60 "
Sub Total		3.0 Watts
Storage Vessel Heat Load		
Conduction losses	Electrical wiring	.10 Watt
	Piping	.50 "
	Supports	.10 "
Multilayer Insulation heat leak, 80 K to 4K		.30 "
Sub Total		1.0 Watt

The primary heat load totals ~ 4.0 Watts
A primary heat load of 4.0 Watts vaporizes 5.7 liters of LHe per hour producing a mass flow rate of 0.2 g/s. Gas specific heat cooling capacity from 5 to 80K is 80 watts. Storage vessel refill rate would be a minimum of 31 hours.
Secondary heat load estimate - Heat intercepted by cold boil off gas to reduce the primary load.

Experiment Lower Vessel:

Conduction losses	Electrical wiring	10.0 Watts
	Beam Tube Heat Station	10.0 "
	Supports	4.0 "
IR Losses	Multilayer Insulation heat shield, 300k to 80k	6.0 "
Sub Total		30.0 Watts
Storage Vessel		
Conduction Losses	Piping	5.0 Watts
	Electrical wiring	2.0 "
	Supports	2.0 "
IR Losses	Multilayer Insulation heat leak, 300k to 80k	4.5 "
Sub Total		13.5 Watts

Secondary Heat Load Total ~ 43.5 Watts

These primary and secondary heat load estimates will be further refined, but the estimates show, with wide margins, that the primary heat load is 80% of the storage vessel's 175 liters/day. And the secondary load of ~ 40 Watts is only 40% of the 100 watt 24 hour refill rate gas boil off. This means that a liquid use of 80% of maximum will provide about twice the secondary mass flow needed to hold the shields and heat station at 80K. The result will be colder shield temperatures which will reduce the heat leak to the primary and reduce liquid use. Calculating the temperature where primary and secondary loads are in balance will be done later.

7.3.2 COOLING

Designers of the RHIC cryogenic system had the foresight to install spare LHe spigots on valve boxes located next to all experimental areas. At 10 o'clock, all trays, supports and sleeves into the tunnel have been installed, so to bring RHIC LHe to the experiment will only take the installation of 150' (45.7 m) of transfer line and a few valves. Boil off gas is returned to the refrigerator via a warm line that sends gas back to compressor suction. The RHIC He refrigerator is the world's largest and even though it's running at about half power, the effect of taking a few hundred liters of liquid to fill the experiment's storage vessel will not be visible to the control room operators. Figure 16 is a plan view drawing showing the run of the LHe transfer line installed in the 10 o'clock area.

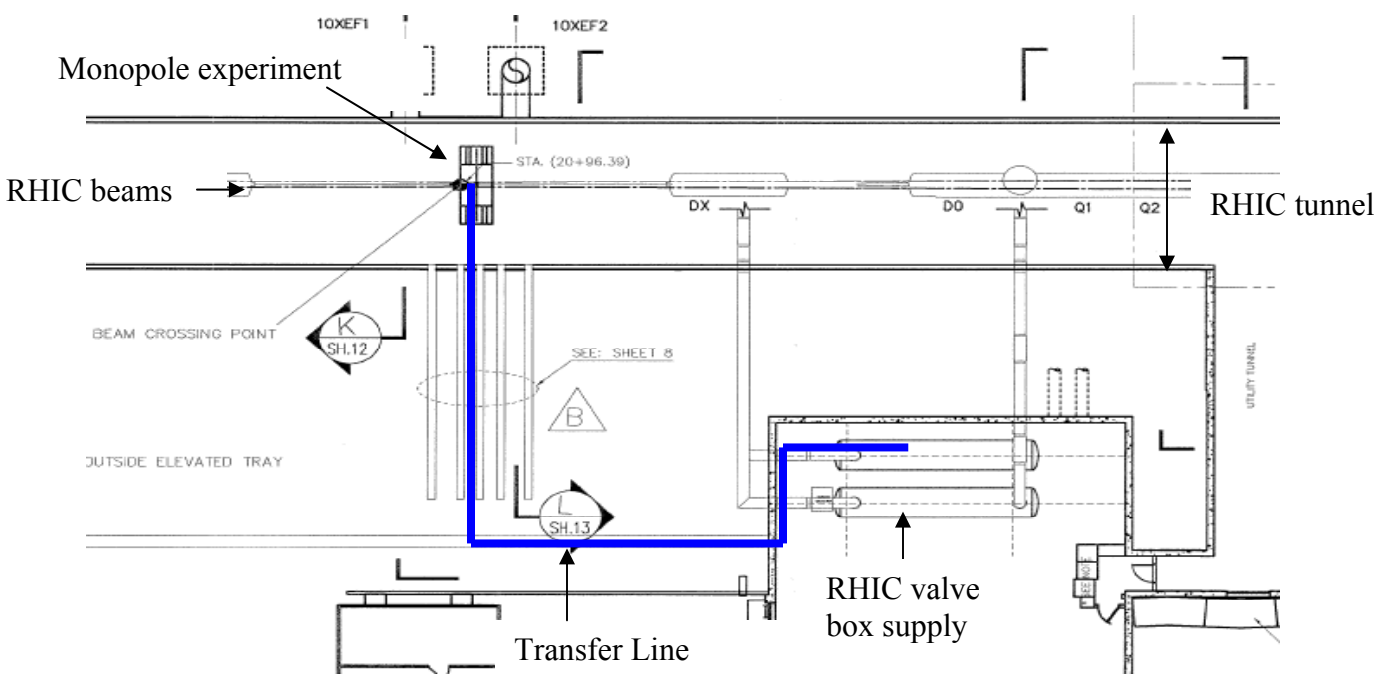

Figure16. RHIC 10 o'clock Transfer line helium supply.

8. FUTURE DEVELOPMENT

We consider two scenarios for the future. In the first, we observe a monopole signal in our feasibility detector. This would be remarkable. This will give us information about the charge but not the mass of the monopole. In order to determine the mass of the monopole, we plan to apply a magnetic field to deflect the monopoles and obtain the g/m ratio.

In the second scenario, we observe no candidate event at all. However, the detector performs satisfactorily, as demonstrated by a clear signal from the magnetic pseudopole of strength equal to that of a monopole with an assumed quantum number. There are two possibilities: there were no monopoles produced in RHIC collisions or, alternatively, we will not have run long enough.

If no monopoles are observed, we plan to approach the Large Hadron Collider management to seek permission to carry out the next phase of the experiment there. This approach explores the formation of monopoles at substantially higher energy than those available at RHIC.

The use of the LHC will clearly advance the monopole search into a new domain. Monopole searches at the LHC have been proposed [21]. However, the proposal uses a plastic track etch detector. This is in sharp contrast to our proposal which relies on the unambiguous magnetic signature of the monopole.

9. SCHEDULE

Monopole Detector Schedule

ID	Task Name	Duration	Start	Finish
1	RHIC Cryo Operation	483 days	11/1/07	6/14/10
2	RHIC Cryo Off	305 days	7/2/07	10/1/10
3				
4	Monopole Project Funding Go-Ahead	0 days	7/1/07	7/1/07
5	Design	65 days	7/2/07	9/28/07
6	1st Approved Dwg's to Machine Shop	0 days	8/15/07	8/15/07
7	Shop Work	88 days	8/16/07	12/17/07
8	Test Gradiometers	10 days	8/15/07	8/28/07
9	Purchase Parts	64 days	8/15/07	11/12/07
10	Purchase Parts Delivery	66 days	9/3/07	12/3/07
11	Install Tunnel Parts/Prep	31 days	9/3/07	10/15/07
12	Assemble Detector Pieces/Leak Test	87 days	9/17/07	1/15/08
13	Control System Preparation	88 days	11/15/07	3/17/08
14	Detector Construction Complete	0 days	2/15/08	2/15/08
15	Cold Test (outside tunnel)	87 days	2/15/08	6/16/08
16	Install in Tunnel	22 days	6/16/08	7/15/08
17	Monopole Detector Installed	0 days	7/15/08	7/15/08
18	Cold test in Tunnel	79 days	7/15/08	10/31/08
19				
20	**Silicon Detectors**	**261 days**	**7/2/07**	**6/30/08**
21	Design	43 days	7/2/07	8/29/07
22	Production	120 days	9/3/07	2/15/08
23	Testing	96 days	2/18/08	6/30/08
24				
25	**Silicon Detectors Electronics**	**261 days**	**7/2/07**	**6/30/08**
26	Design	43 days	7/2/07	8/29/07
27	Production	120 days	9/3/07	2/15/08
28	Test	96 days	2/18/08	6/30/08
29				
30	**SQUID**	**261 days**	**7/2/07**	**6/30/08**
31	Purchase Samples	43 days	7/2/07	8/29/07
32	Total Purchase	120 days	9/3/07	2/15/08
33	Testing	96 days	2/18/08	6/30/08
34				
35	**SQUID Electronics**	**261 days**	**7/2/07**	**6/30/08**
36	Purchase Samples	43 days	7/2/07	8/29/07
37	Total Purchase	120 days	9/3/07	2/15/08
38	Testing	96 days	2/18/08	6/30/08

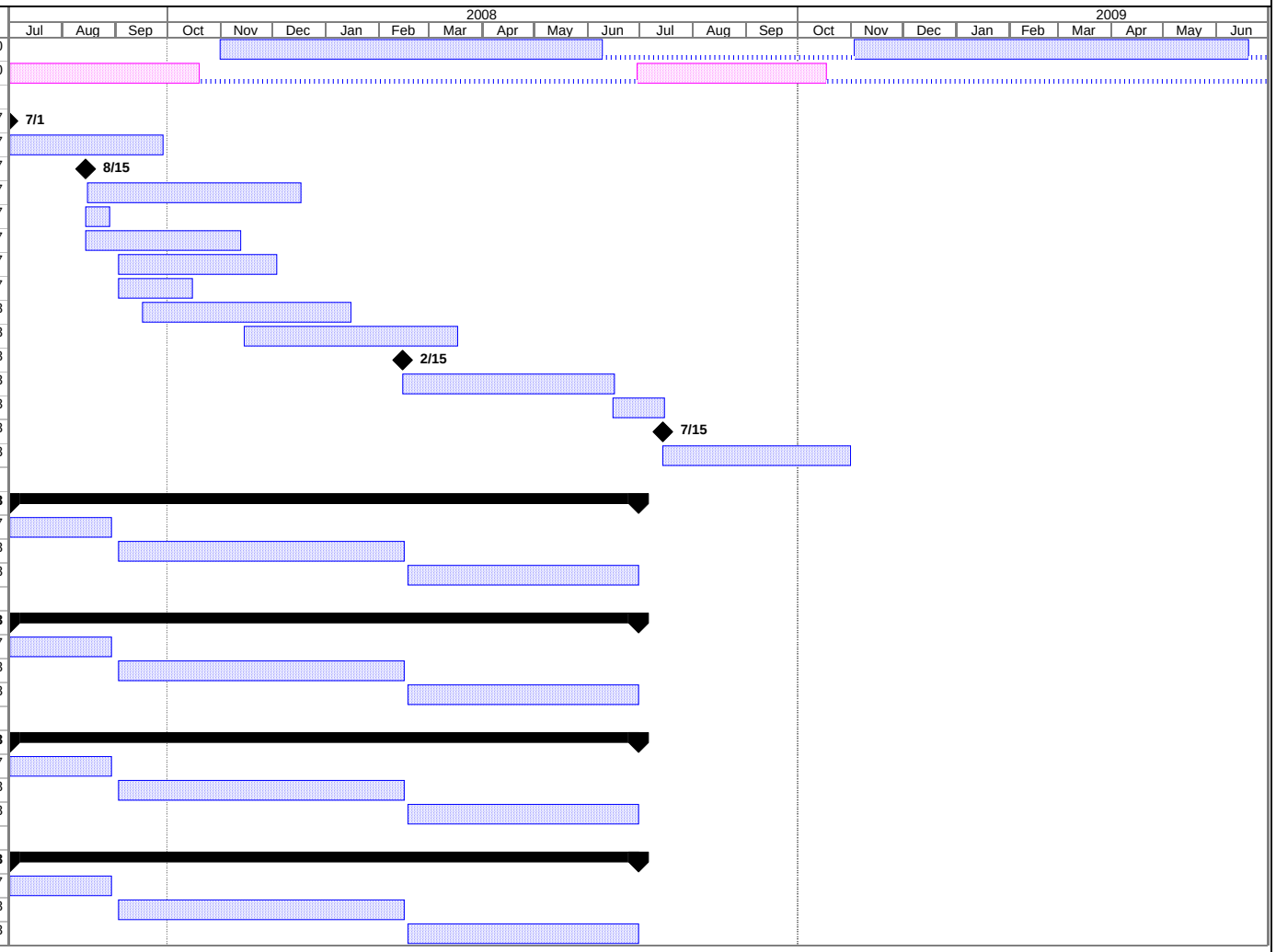

10. COST ESTIMATE FOR CONSTRUCTION AND SETUP OF THE EXPERIMENTAL APPARATUS

Materials and Supplies:

1. Detector cryostat and refrigeration system		$390k
2. Magnetic detection system (gradiometers, SQUIDS, control and signal processing electronics)		$190k
3. Silicon detector system		$220k
4. Data Acquisition (DAQ)		$80k
	Subtotal:	$880k

Manpower:

1. S&P	2.5 FTE	$650k
2. Other (designer and technical specialists)	3.5 FTE	$630k
3. C-AD costs		$180k
	Subtotal:	$1,460k
	Project total:	$2,340k

Notes:

1. Materials and Supplies include 25% contingency.
2. Cost estimates for materials and supplies are based on vendor quotes where applicable (SQUIDS with control electronics), engineering design experience, prior experience with similar devices (silicon detectors, vacuum and cryogenic components).
3. Labor cost includes fringe, org. burden, and BNL overhead.
4. Collider-Accelerator Department costs for the experiment is included.

11. REFERENCE

1. G. ‘t Hooft, Nucl. Phys. B79, 276 (1974); A.M. Polyakov, JETP Lett., 20, 194 (1974
2. P.A.M. Dirac, Proc. Roy. Soc. London, A133, 60 (1931)
3. M. Ambrosio et al., arXiv:hep-ex/0207020, 2, July 9 (2002); F. Balestra et al., 29th Intnl. Cosmic Ray Conf, Pune, 101-106 (2005)
4. S. Gavin et al., Int.J.Mod.Phys.A10:2961-2998, (1995)
5. O. Martin, A. Schafer, M. Stratmann and W. Vogelsang; Phys. Rev., D60, 117502 (1999)
6. G.R. Kalbfleisch et al., Phys. Rev. Lett. 85, 5292 (2000)
7. K.A. Milton, Rep. Prog. Phys. 69, 1637 (2006)
8. G. Baur hep-ph/0112239 (2001)
9. A.J. Baltz and M. Strikman, Phys.Rev. D, 57, 548 (1998)
10. G. Giacomelli and L. Patrizi, hep-ex/0506014 and hep-ex/0302011
11. D. Kharzeev et al., nucl-th/0012025, (2000); D. Kharzeev et al., Nuclear Physics A 747, 609 (2005)
12. G.R. Kalbfleisch et al., Phys. Rev. D.69, 052002 (2004)
13. A. Abulencia et al., Phys. Rev. Lett. 96, 201801 (2006)
14. I.I. Gurevich . et al., Phys. Lett. 38B, 549 (1972),
    I.I. Gurevich et al., Phys. Lett., 31B, 394 (1970)
15. R.A. Carrigan.et. al. Phys Rev D, v10, 3867 (1972)
16. SQUID Handbook, J. Clarke and A.I. Braginski, eds., Wiley-VCH, Berlin, Germany, 2004; R. Kleiner, D. Koelle, F. Ludwig and J. Clarke, “Superconducting Quantum Interference Devices: State of the Art and Applications”, Proc. IEEE,. 92, NO. 10, Oct. 2004
17. D. Drung, H. Mattz and H. Koch Rev. Sci. Instrum. 66 (4), April 1995; D. Drung, C. Aßmann, J. Beyer, M. Peters, F. Ruede, and Th. Schurig, IEEE_Trans Applied Super cond VOL. 15, NO. 2, June 2005; S. Bechstein, D. Drung, F. Petsche, M. Scheiner, C. Hinnrichs, H.-J. Barthelmess, and Th. Schurig, IEEE Transactions On Applied Superconductivity, Vol. 15, No. 2, June 2005; D. Drung (PTB-Berlin) “HTS and LTS dc SQUID Electronics” ISEC 03 available at: http://www.tip.csiro.au/ISEC2003/talks/IWe2.pdf
18. S. Rescia, "Low Noise Electronics for Ionization Detectors with Emphasis on Noble Liquid Calorimetry for High Energy Physics", Ph.D. Thesis, University of Pennsylvania, 2000.
19. J. Ziegler, C.C. Tsuei, C.C., Chi, C.D.Tesche, P. Chaudhari, P., and K.W. Jones, Phys Rev., D28, 1793 (1983)
20. W.E. Cleland et. al., 6th International Conference on Calorimetry in High-Energy Physics (ICCHEP 96), Rome, Italy, 8-14 Jun 1996. Published in *Frascati 1996, Calorimetry in high energy physics* 849-860
21. MOEDAL (Monopole and Exotic Particle Detector): http://web.cern.ch/moedal/
22. S. Graf et al., Phys. Lett. 262B, 463 (1991)
    A.I. Studenkin. Sov. J. Part. Nucl. 21, 259 (1990)
    E. Picasso NATO Advanced Study Institute, Dr. B, Physics, 80, 441(1981).
    G.W. Bennett et al., Physics Review, D73, 072003-1 (2006)
23. I.F. Ginzburg and S.L. Panfil Sov. J. Nucl. Phys. 36 850 (1982)

I.F. Ginzburg and A. Schiller Phys. Rev. D 57 6599-603 (1998)
I.F. Ginzburg and A. Schiller Phys. Rev. D 60 075016 (1999)
B. Abbott et al., Phys. Rev. Lett. 81 524 (1998)
24. M. Acciarri et al Phys. Lett. B 345 609 (1995)
A. De Rujula Nuclear Physics, B435 257 (1995)
25. Y.M Cho and D.Maison hep-th/9601028 (1996), Phys. Lett. B391 p.360, 1997.,Y.M.Cho and K. Kimm hep-th/9705213
W. Troost and P. Vinciarelli Ref.TH. 2195-CERN (1976)
26. T. Banks et al., Phys. Lett. B212, 45 (1988)
E.Witten; hep-th/0212247
27. G. 't Hooft, Nucl. Phys. B 79, 276 (1974).
M. Polyakov, JETP Letters 20, 430 (1974).

APPENDIX

A.1 SECONDARY ELECTRONS

A.1.1. INTRODUCTION

The presence of backgrounds or noise that plagues all RHIC experiments [A1] needs to be carefully considered in this experiment, especially in view of the small amplitude of the expected signal and the presumably extreme scarcity of such events. Triggering or gating with ancillary detectors to limit the observation to short time intervals containing central collisions is one possibility. Compared to detectors designed to detect charged particles, we should be less sensitive to direct hits by reaction products, by gamma rays or by beam halo particles. Here we explore a type of possible noise, specific to our type of detector, which is caused by electromagnetic waves induced in the experimental chamber by the sudden appearance of charged particles. The effects produced by the beam bunches and by beam-generated electron clouds were addressed in the main text and are not considered here. Here we consider the effects of potentially a large number of secondary electrons generated when charged reaction products impinge on the chamber walls or on other surfaces. We shall first address the number, nature, and angular distribution of these particles, then the expected secondary electron yields per particle-impact, and finally the resulting estimated order of magnitude of the generated charge. We shall conclude that this effect will not be a significant issue.

A.1.2 ANGULAR DISTRIBUTION OF CHARGED PARTICLES FROM AU+AU COLLISIONS

We will consider the worst case, i.e. a central gold-gold collision at 200 GeV/u

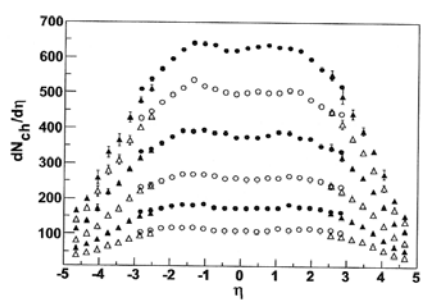

FIG. 1: Distributions of $dN_{ch}/d\eta$ for centrality ranges of, top to bottom, 0-5%, 5-10%, 10-20%, 20-30%, 30-40%, and 40-50%. The SiMA and BBC results are indicated by circles and triangles, respectively. Statistical errors are shown for all points where they are larger than the symbol size.

Figure A.1.1 (copied from reference [A2]).

center-of -mass energy. We start with the data [A2] for charge particle production as function of pseudorapidity η shown in Figure A.1.1.
Here $\eta = -ln\ [tan\ (\theta/2)]$ where θ is the angle between the particle emission and the beam. Using this equation, and the numerical data [A1] for the topmost curve of Figure.A.1.1 [A2] to obtain the angular distribution shown in Figure A.1.2. This is the flux, i.e. particles per steradian (dN/dΩ) as function of θ.

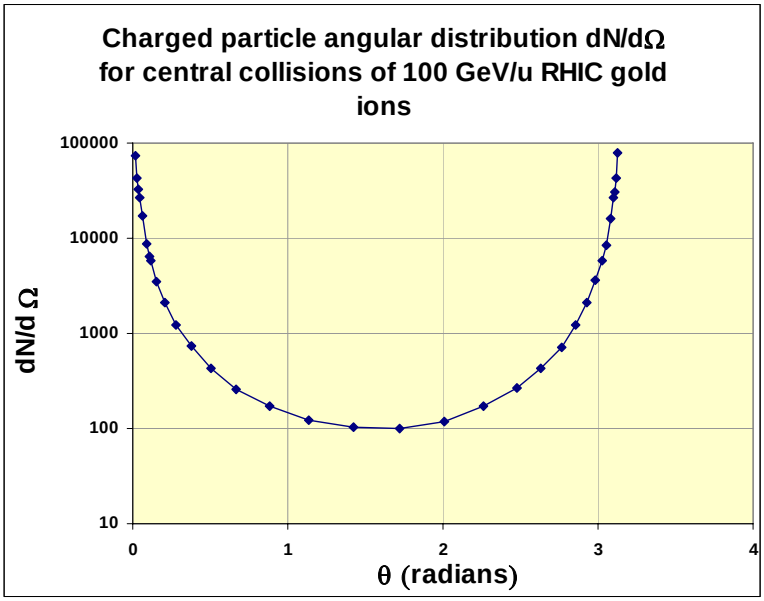

Figure A.1.2. Charged particle distribution.

We see that the distribution is very strongly peaked at angles close to the beam, and that around 90 degrees the flux is close to 100 particles per steradian per central collision. Even going as far as ± 1 radian (± 57°) away from perpendicular emission, the average flux is still not more than ~120 particles per steradian.

Most of the particles are energetic, minimum-ionizing pions (~80%) [A1]. The remainder are kaons (also minimum ionizing) and protons (< 10%) of which a small percentage may be of low enough energy to be up to ~twice minimum ionizing. For our rough estimates we will simply assume all these charged particle to be minimum ionizing. This approximation will be used in the next section to estimate secondary electron yields.

A.1.3. SECONDARY ELECTRON YIELD ESTIMATES

There are few experimental results for the angular dependence of secondary electron yields for energetic ions, and none that we know of for pions or kaons. Figure A.1.3 shows the angular dependence [A3] of secondary-electron yields for 28-MeV protons, 126 MeV oxygen-ions and 182-Mev gold ions incident on stainless-steel surfaces. Here the angles are measured with respect to the normal to the surface. The maximum

yields are obtained for near grazing collisions (90°), and for angles <89° the distributions show approximately a 1/cos angular dependence.

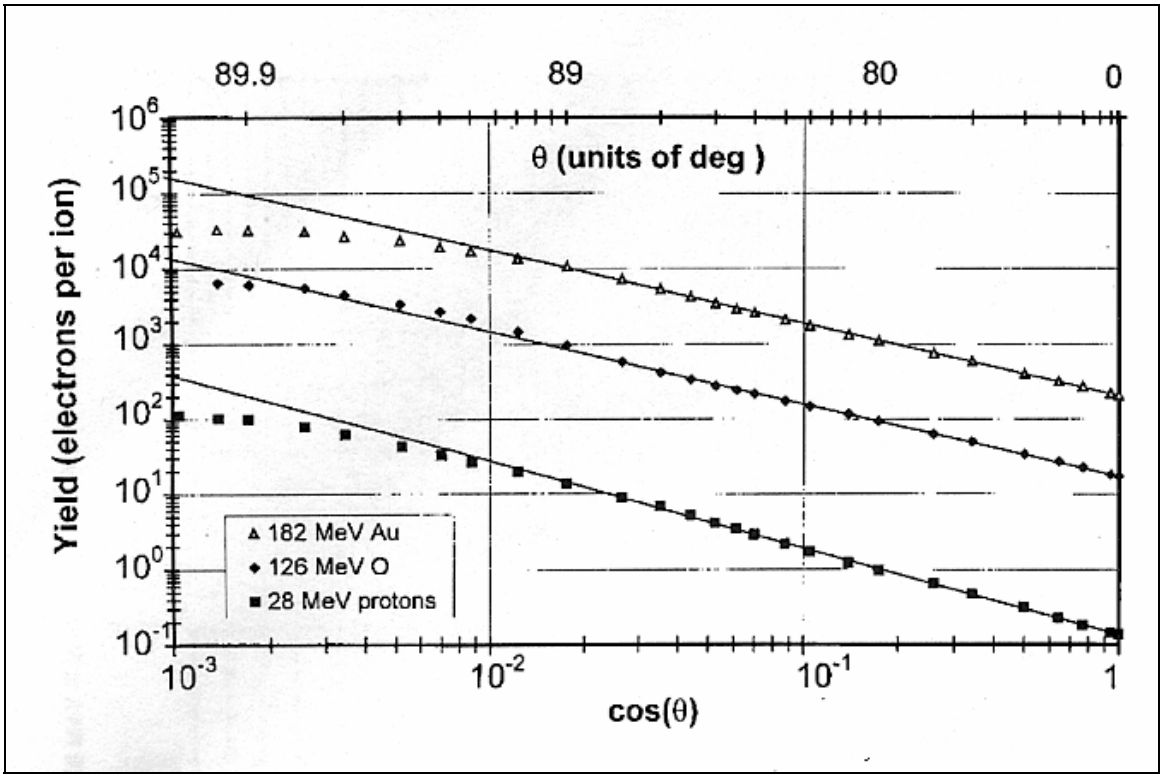

Figure A.1.3 Angular dependence of secondary electron yields for three energetic ion beams incident on stainless-steel [A3].

For light ions the yields at a given angle scale approximately as the specific energy loss dE/dx (see [A3] and references therein). We will assume that this rule also applies to energetic pions and kaons. All these particles from gold-gold collisions, including the protons, can be assumed to be nearly minimum ionizing as discussed above. We therefore estimate their secondary electron yields by scaling the proton data of Figure A.1.3 by the ratio 1.45E-3/1.34E-2 of the dE/dx values for minimum ionizing particles and for 28 MeV protons in iron respectively [A4]. The result is shown in FigureA.1.4.

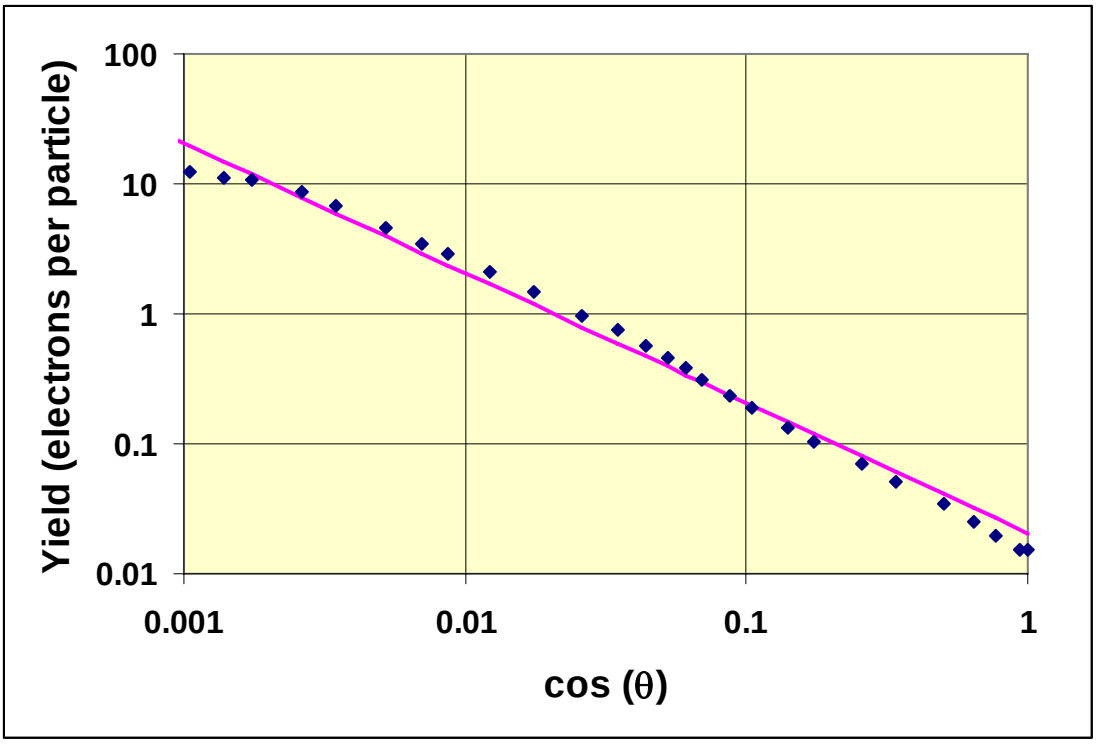

Figure A.1.4 Estimated secondary electron yields as function of angle for minimum ionizing charged particles incident on stainless steel, derived form the data [A3] shown in Figure A.1.3. The straight line shown here is proportional to *1/cos (θ)* rather than the slightly more complicated function [A3] used to fit the data of Figure A.1.3.

Now we have all the necessary ingredients, at least in principle, to estimate the number of secondary electrons that will be generated in our apparatus for a given geometry of the surfaces exposed to impacts by particles originating in the interaction region.

A.1.4. SECONDARY ELECTRON PRODUCTION ESTIMATES

Using the charged particle angular distribution (Figure A.1.2) and the estimated secondary electron yields (Figure A.1.4) we could calculate the average electron production from a given surface element due to a central collision at a given point of the interaction region. Then we would calculate a weighted average over the luminosity distribution of the interaction region and integrate over the surface elements exposed to the particles.

For now we will follow much cruder approach to obtain an estimated upper limit for the number of secondary electrons. The solid angle for accepting particles into the experimental volume as defined by the slot in the beam pipe, the valve and the trapezoidal transition piece may vary in the final design, but will probably remain below 5% of 4π, i.e. below ~0.6 steradians. As we saw in section A.1.2, we will have ~120 particle per steradian in this angular range, and therefore the number of particles entering the experiment will be ~72 for a central collision. Even if each of these particles generated the maximum ~10 electrons shown in Figure A.1.4, we would still end up with only ~700 electrons or $\sim 10^{-16}$ C. The real number will be much smaller because the particles will hit at a variety of angles, and as soon as we move away from grazing incidence by even as little as one degree, the yield is already reduced by more than an order of magnitude.

There are of course large uncertainties in these estimates. For example the grazing incidence yields for energetic pions and kaons may be significantly different from the estimate based on scaling from 28 MeV protons. However, the upper limits we obtain are so small that we may conclude that these secondary electrons will not affect the experiment.

A.1.5 REFERENCES

[A1] C. Chasman, private communication.

[A2] BRAHMS Collaboration, Phys. Rev. Letters. 88, 202301 (2002) Issue 20, 2002

[A3] P. Thieberger, A. L. Hanson, D. B. Steski, V. Zajic, S. Y. Zhang, and H. Ludewig, Phys. Rev. A 61, 042901 (2000).

[A4] SRIM code, J. F. Ziegler, SRIM.com, 1201 Dixona Dr.Edgewater, MD, 21037, USA

A.2 THERMAL ANALYSIS

A.2.1 THERMAL ANALYSIS OF THE SUPERCONDUCTING GRID.

The two superconducting grids enclosing the lead /niobium superconducting box are made of 1mm thick copper with niobium deposited on top. They comprise of 1 cm squares with 0.5 mm wide walls. This configuration is easily achieved by using an etching technique. A thermal analysis, where a heat load of 24 W/m^2 is applied and the edge is held at 4 K, shows that the center of the grid reaches 5 K, well below the superconducting transition temperature of niobium. Although Figure A.2.1 shows one quarter of the model for ease of computation, the grid is made in one piece. This grid geometry results in a 90% optical transparency.

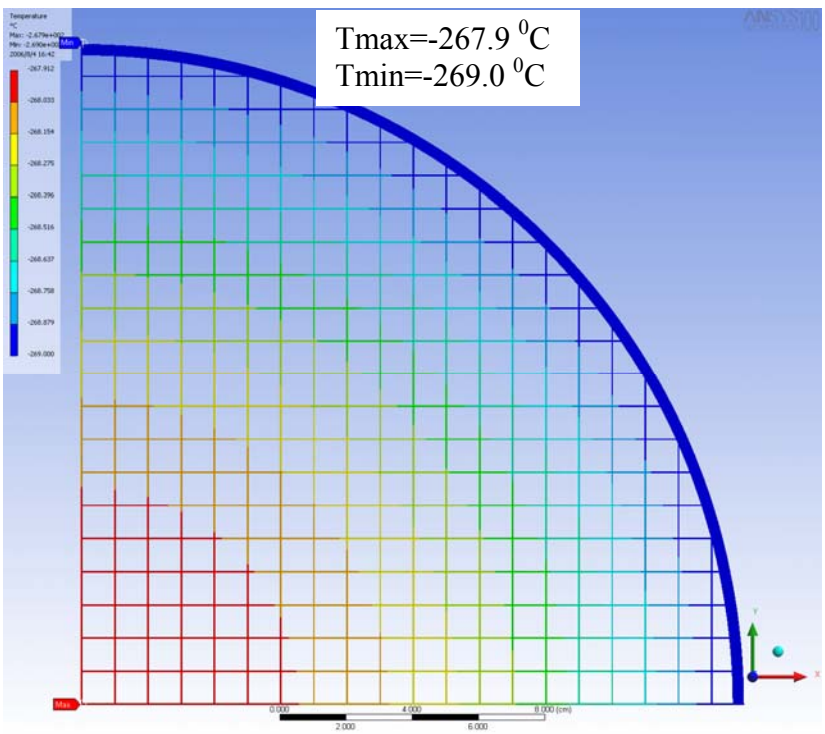

Figure A.2.1 Thermal analysis of the superconducting grid.

A.2.2 THERMAL ANALYSIS OF THE GRADIOMETER

The gradiometers are made of 4 separate silicon quarters coated with 100 Angstrom Cr and 2000 Angstrom Cu. A heat load of 24 W/m^2 is applied and the cooling is provided at two spots (held at 4K) per quadrant by means of soldering copper braids to the copper surface. A parametric study showed that the temperature gradient remains approximately 1K or less with the order of the gradiometer (first to fourth order) or the width of the spokes (1mm to 2mm). This is a consequence of the fact that additional material improves conduction but increases the heat load. There is one significant parameter, the thickness, which we find must be at least 3mm to keep the temperature at the center below 5K,

required to be below the superconducting transition of a niobium film which makes the gradiometer operate. The two Figures, A.2.2 and A.2.3, map the temperature distribution across a second and fourth order gradiometer. The temperature increase at the center is 1K in Figure A.2.2 and 0.5K in Figure A.2.3.

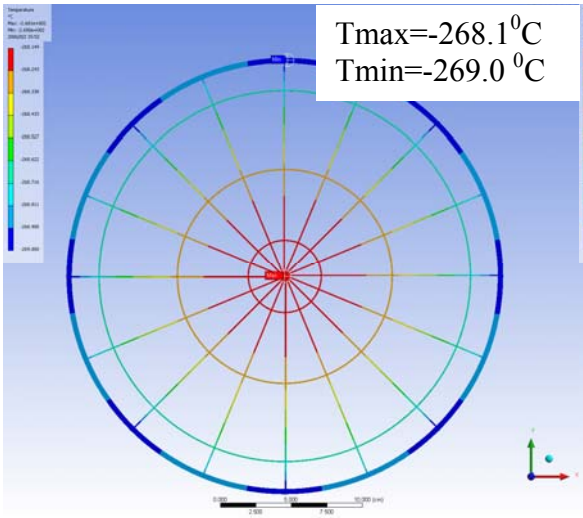

Figure A.2.2 Second order gradiometer.

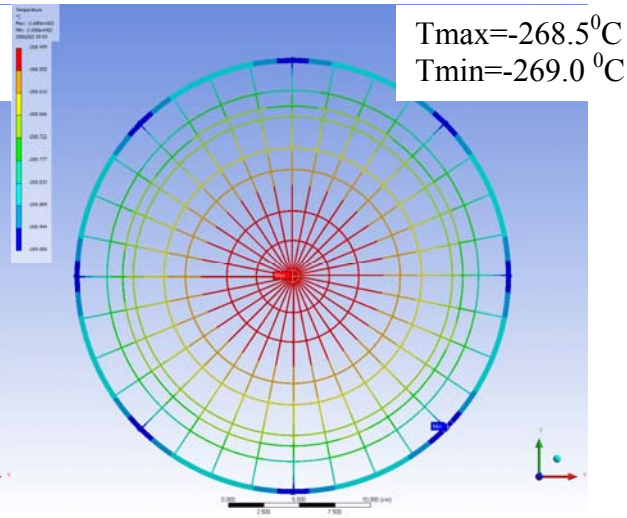

Figure A.2.3 Fourth order gradiometer.

A.3. STRUCTURAL ANALYSIS

One of the concerns we have is the deformation of the gradiometer during operation by a static or dynamic load. This can introduce random noise in the output of the gradiometer. Hence we have carried out a structural analysis of the gradiometer under different loading conditions.

A.3.1 STRUCTURAL ANALYSIS OF THE GRADIOMETER UNDER GRAVITY

When the gradiometer is held at two edges (1/8 th of the total circumference) at the bottom, deformations under gravity load amount to 0.03mm on the top. Equivalent stresses are 0.13 MPa for silicon, which has a yield strength of 120 MPa. This is the worst case scenario and is tolerable. Our gradiometers will be uniformly supported along their edges. Hence, we will ignore the effects of gravitational loading in designing the arrangement of the gradiometer wiring.

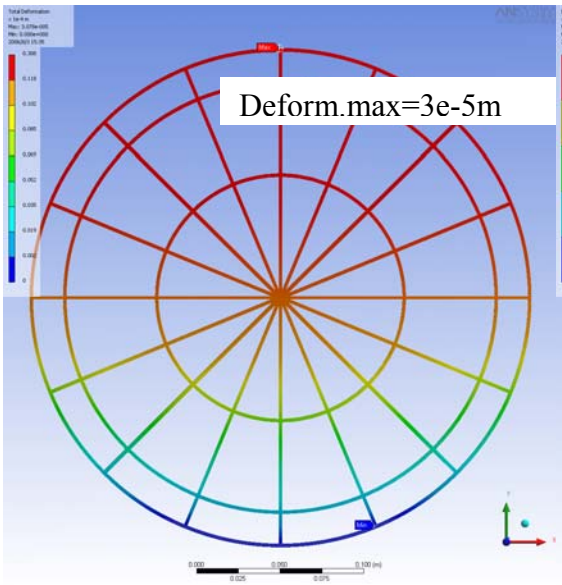

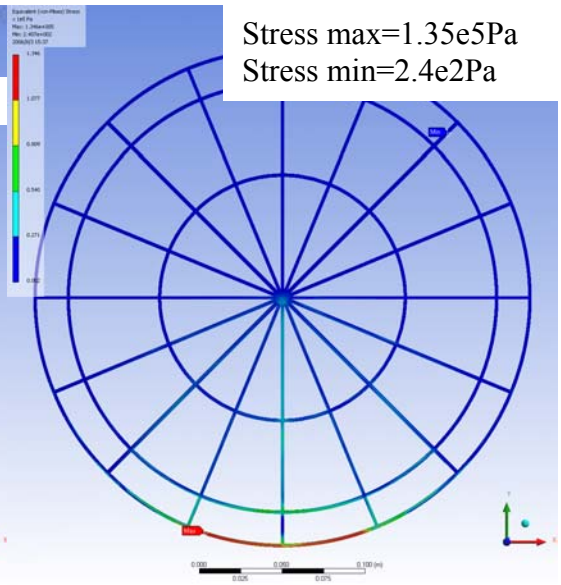

Figure A.3.1. Deformation of the gradiometer. Figure A.3.2. Stresses on the gradiometer.

A.3.2 MODAL AND HARMONIC ANALYSIS OF THE SILICON GRADIOMETER AND ITS SUPPORT

The first three natural frequencies of the gradiometer, where the 4 quarters are assumed to form one solid piece, uniformly supported at the edges are 131.3 Hz, 341.5 Hz, 343.7 Hz. Below, we show the first mode (figure A.3.1) and the deformation (Figure A.3.2) when excited by a 1N force with frequency identical to the first natural frequency applied at the center of the gradiometer. A 0.2 mm deformation and corresponding stresses of 6 MPa result from this load.

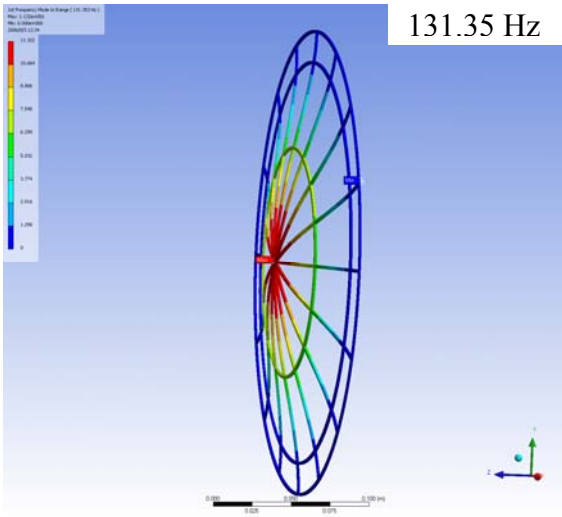

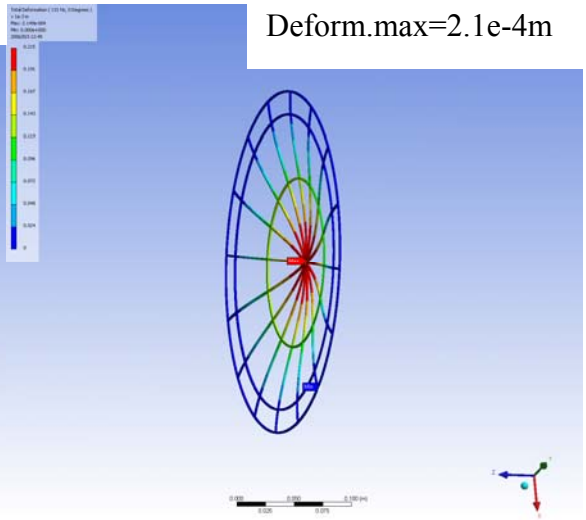

Figure A.3.3.First mode of vibration.

Figure A.3.4. Deformations of gradiometer under harmonic excitation.

The Figures below show the second and third modes.

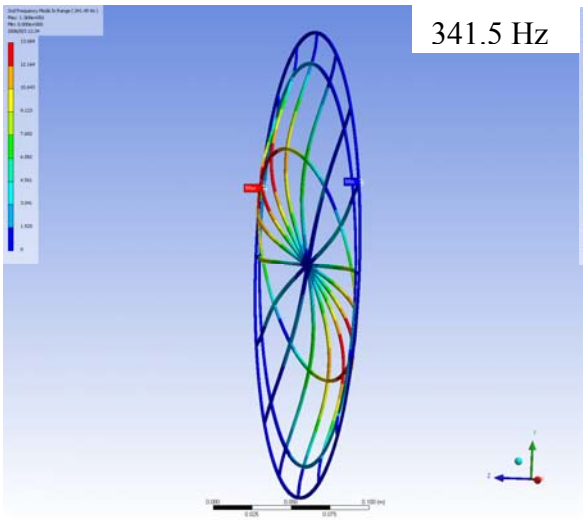

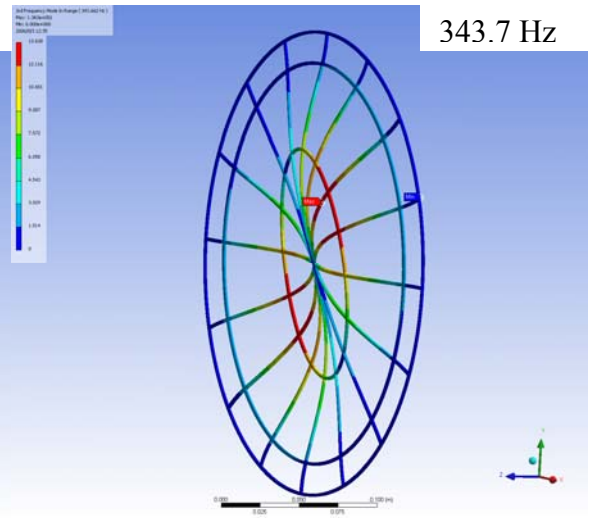

Figure A.3.5. Second mode of vibration.

Figure A.3.6. Third mode of vibration.

This deformation is an order of magnitude larger than the static load under gravity discussed above. Hence, we have provided supports to minimize the displacements caused by vibrations. The gradiometer is supported by a ring with a cross in the center.
The natural frequencies of the support rings fixed at the tabs are now 544.7 Hz, 666.6 Hz, 1114.8 Hz. The first mode and the deformation when a 1N harmonic force at the first resonance frequency is applied at the center are shown below. A deformation of 10^{-8} m is obtained, five orders of magnitude less than if the stiffening ring with the cross were absent. Our design of the gradiometer therefore incorporates a ring with a cross for stiffening.

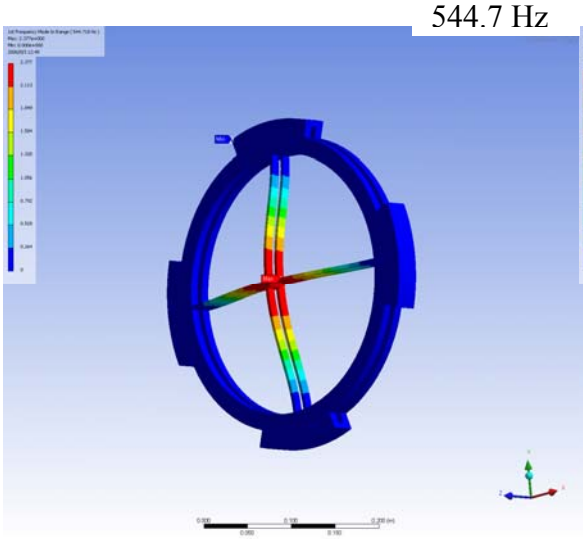

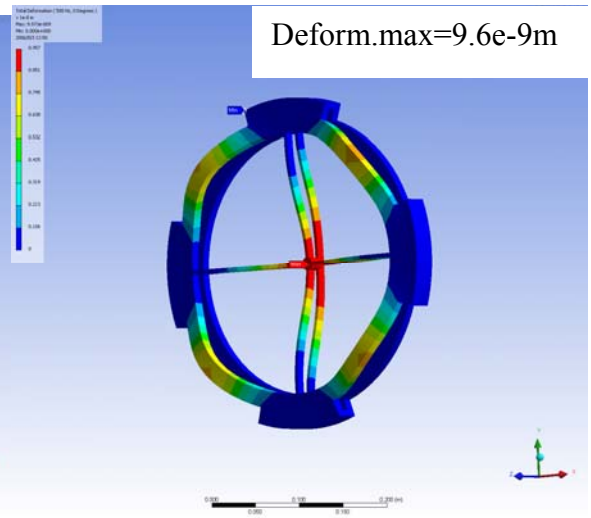

Figure A.3.7. First mode of support ring.

Figure A.3.8. Deformations of support ring under harmonic excitation.

The next two Figures show the second and third mode.

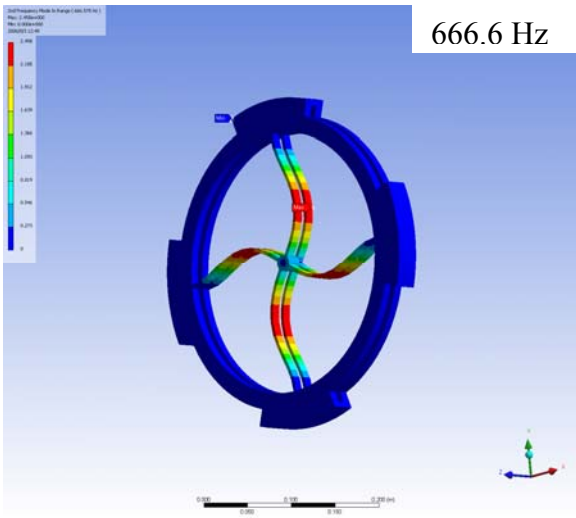

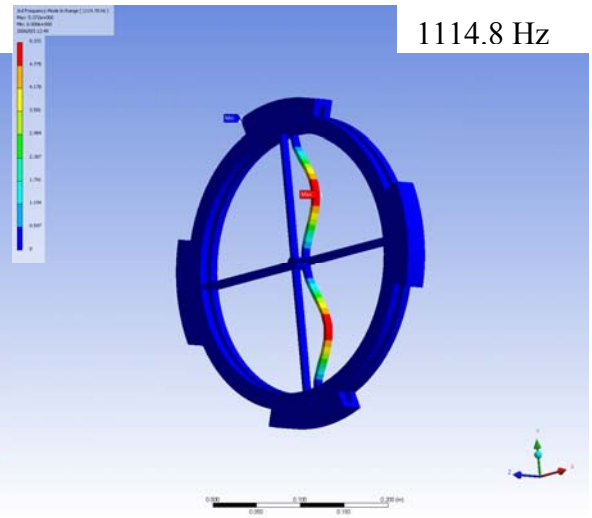

Figure A.3.9. First mode of support ring.

Figure A.3.10. Deformations of support ring under harmonic excitation.

A.4. MAGNETIC SHIELDING

Magnetic shielding is provided by 3 mu-metal layers and two superconducting shields which both shield and pin the residual magnetic fields. Here we describe the shielding provided by the mu-metal for our experimental geometry.

The 3D magnetic analysis is performed by first creating a solenoid with proper parameters that would produce a uniform field of 0.5 Oe, the earth's magnetic field. The solenoid (represented by a single loop in Figure A.4.1.) is large enough with respect to the mu metal shield and oriented to align the uniform field with the axis of the shield (quarter cylinder with slot for trapezoidal transition piece on one face), a worst possible case. To satisfy the numerical analysis requirements an air "enclosure" with 2 planes of symmetry is introduced (rectangular box). The boundary conditions that the flux be parallel to the planes of symmetry are added.

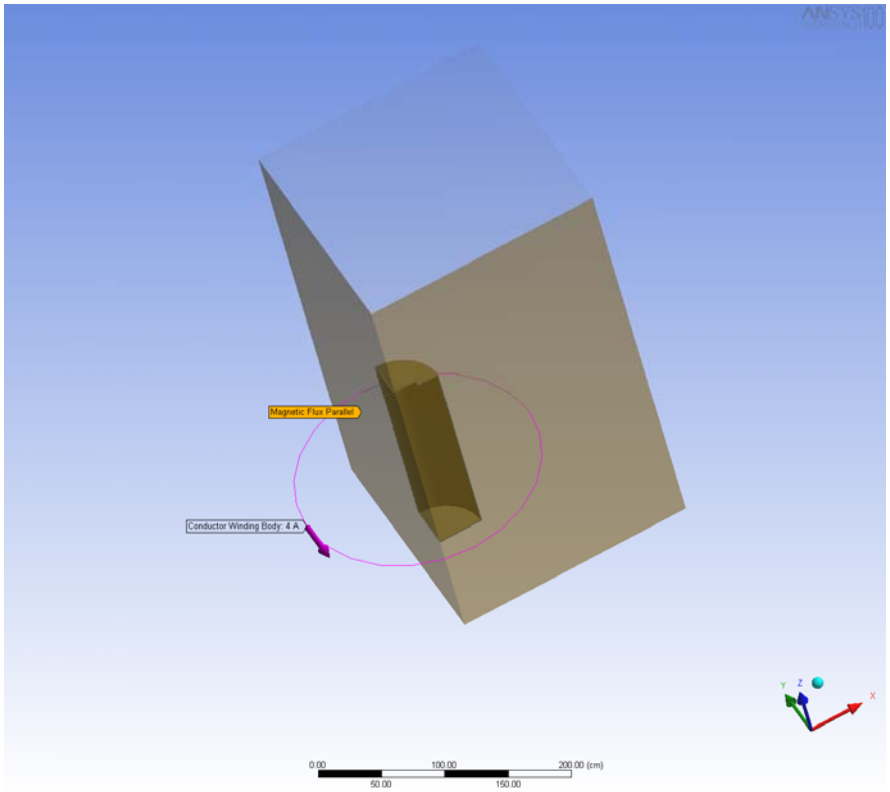

Figure A.4.1. One quadrant of Shield.

The Figures below are views along the axis of the shield for the case where there is a hole due to the trapezoidal transition piece (Figure A.4.2.) and the case with no hole (Figure A.4.3) for comparison. The mu metal shield 1 cm thick reduces the external field by three to four orders of magnitude (0.5 Oe to 5e-4 Oe). The presence of the hole affects about half of the interior of the shield. The shielding effect is reduced by one to two orders of magnitude when the hole is present. In both cases, in the region where the gradiometers are located the residual field is about 5e-4 Oe.

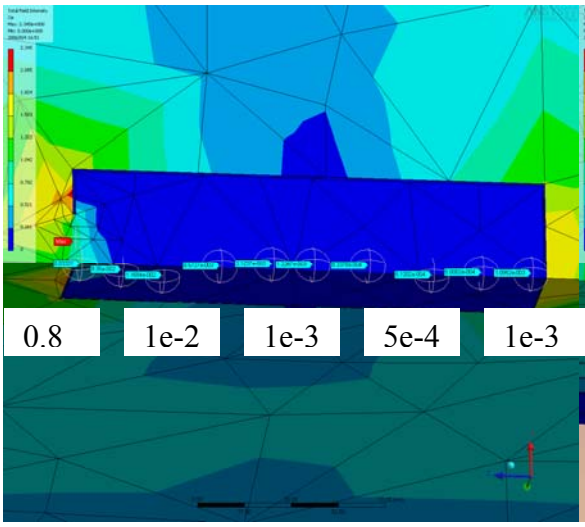

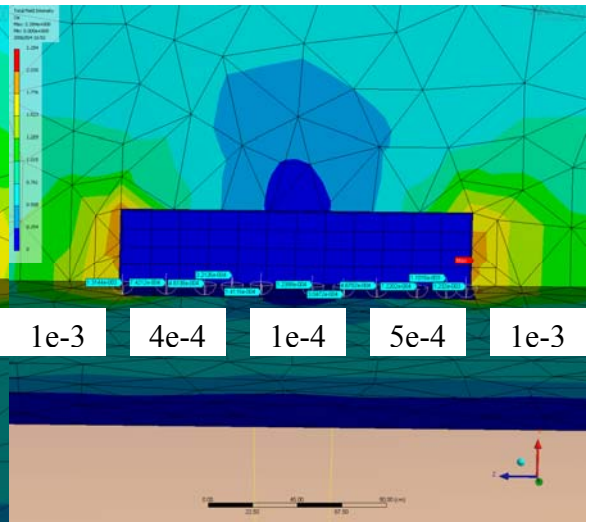

Figure A.4.2. Shield with hole.

Figure A.4.3. Shield without hole

We have also performed a 2D analysis to investigate the optimal number of layers and Shield configuration to provide maximum shielding, keeping in mind that mu-metal comes In 1mm and 1.2mm thickness. One to four shields of dimension 1mm to ½ mm thick spaced 1 to 2 mm away studied as possible configurations. The best reduction in field by factor $2x10^{-3}$ occurred for three shields which are 1mm thick and spaced 2mm apart.